



Mechanical and corrosion characteristics of heat-treated wire arc additive manufactured parts of Inconel[®] 625 superalloy

Fábio Henrique Silva Delfino¹ · Guilherme Yuuki Koga² · Thiago R. F. Cavalcante³ · Douglas Bon³ · Joseane Giarola³ · Jiajia Shen⁴ · Joao Pedro Oliveira⁴ · Éder Sócrates Najar Lopes¹ · Julian Arnaldo Avila⁵

Received: 28 March 2024 / Accepted: 20 August 2024
© The Author(s), under exclusive licence to Springer Nature Switzerland AG 2024

Abstract

Inconel[®] 625 alloy (IN625) has been used extensively in aerospace, petrochemical, chemical, and marine applications due to its attractive combination of high tensile strength and excellent corrosion resistance. However, manufacturing components of IN625 is still challenging given the shape complexity and the high associated production costs ascribed to the excess metal removal in subtractive manufacturing techniques. Therefore, wire arc additive manufacturing through the direct energy deposition (DED-WA) technique had a growing interest due to gas metal arc welding with regulated metal deposition (GMAW—RMD[™]) of IN625. In this work, a computer numerical control (CNC) device was developed to perform the deposition of layers of an ErNiCrMo-3 wire to produce rectangular geometries with external dimensions of 210 × 100 × 60 mm and 10 mm thickness walls. Samples were sectioned and had their microstructural and corrosion resistance assessed. Other samples were heat treated and mechanically and electrochemically tested in two conditions: (i) stress relief (SR) and (ii) SR followed by solubilization (SR + S), aiming to mitigate the harmful effects of phases formed during DED-WA or heat treatments, such as δ -phase. Thin-walled components, 210 × 100 × 60 mm, and 10 mm, were successfully fabricated by wire arc additive manufacturing through the direct energy deposition (DED-WA) technique. The as-build conditions presented ultimate tensile strength (716 MPa), large elongation fracture ($\geq 35\%$), and intermediate fracture toughness (> 1.25 mm). The stress relief (SR) heat treatment improved mechanical properties (YS of ~ 450 MPa and UTS of ~ 750 MPa). However, the lowest elongation and fracture toughness ($\geq 30\%$ and > 0.5 mm) were presented. On the other hand, the additional solution treatment (SR + S) improved the elongation and fracture toughness ($\geq 30\%$ and > 1.5 mm) regarding the AB and SR conditions. The corrosion resistance of all the conditions was higher than the one shown by the wire and comparable to the wrought IN625 alloy at the SR and SR + S conditions.

Keywords Additive manufacturing · Superalloys · Characterization · Heat treatment · Mechanical behavior · Corrosion

1 Introduction

Processing alloys through additive manufacturing (AM) enables them to achieve several benefits, such as reducing production time and costs, reducing waste, easing

automation, and producing near-net shape components [1]. The process heat input distinguishes the AM processes of metals from the deposition sources. For example, the ISO/ASTM 52900:2021 standard divides AM processes into seven categories, where metallic alloys, powder bed fusion

✉ Guilherme Yuuki Koga
gykoga@ufscar.br

✉ Julian Arnaldo Avila
julian.avila@unesp.br

¹ Faculdade de Engenharia Mecânica, Universidade de Campinas (UNICAMP), Campinas 13083-860, Brazil

² Departamento de Ciencia e Engenharia de Materiais, Universidade Federal de São Carlos (UFSCAR), São Carlos 13565-905, Brazil

³ Departamento de Engenharia de Materiais, Universidade de São Paulo (USP), Escola de Engenharia de São Carlos, São Carlos 13563-120, Brazil

⁴ CENIMAT/I3N, Department of Materials Science, NOVA School of Science and Technology, Universidade NOVA de Lisboa, 2829-516 Caparica, Portugal

⁵ Faculdade de Engenharia, Câmpus de São João da Boa Vista, Universidade Estadual Paulista (UNESP), São João da Boa Vista 13876-750, Brazil

(PBF), binder jetting (BJ), and directed energy deposition (DED) are the most important [2]. PBF includes laser PBF (PBF-LB) and electron beam melting (PBF-EB), while DED has laser DED (DED-LB), plasma arc (DED-P), and wire arc additive manufacturing (WAAM or DED-AW) [2]. PBF is typically used for parts requiring greater precision [2], while DED prioritizes productivity.

IN625 has been widely used in aerospace, petrochemical, chemical, and marine applications due to its attractive combination of high tensile strength and excellent corrosion resistance [3]. This basket of properties makes IN625 a prime choice for many applications ranging from cryogenic to high-temperature environments, where strict mechanical/functional requirements are requested [4]. However, the production of IN625 components is still challenging. Several studies regarding PBF-LB and DED-LB processes have been published. Nevertheless, the research literature on IN625 components manufactured by DED-AW, especially with gas metal arc welding (GMAW) with regulated metal deposition (RMDTM), is limited. Regarding DED-AW on IN625, most of the works have been reported in conventional GMAW machines [5, 6], others with cold metal transfer (CMT) [7–10], and the only one developing the window processing for single passes using RMDTM [11]. Given the growing interest in additive manufacturing of IN625 components [7, 8], further research on DED-AW is essential, i.e., to better establish the advantages and disadvantages of using their variants, such as CMT or GMAW-RMDTM. Furthermore, the solidification process of a welded IN625 part is accompanied by the segregation of alloying elements, such as Nb and Mo [1], which requires precise control of the deposition technique and heat input, which favors the use of GMAW-RMDTM due to its lower heat input and high deposition rate [11].

The post-processing steps after AM are usually undesirable because they increase the production time and the cost of the fabricated components. Still, surface quality could be better for DED processes, and machining operations are needed [2]. Two types of heat treatment are recommended for additively manufactured IN625 components: stress relief (SR) and solubilization (S). The SR is recommended for large components to reduce residual stresses that might change the parts' geometries after cutting them from the building platform [12]. Some authors recommend using 870 °C for 1 h [13, 14]. However, between 650 and 1050 °C, a complete displacement of the time–temperature–transformation happens, accelerating δ -phase formation (Ni_3Nb) in IN625 PBF-LB [15, 16]. Based on that study, the best option is to use 800 °C for 1 h or longer to reduce residual stresses, as reported with improved yield strength and reduced elongation to fracture in a previous study processing the same alloy by DED-LB

[14]. On the other hand, solubilization treatments aim to reduce or fully dissolve potentially formed deleterious phases, such as the δ -phase. For example, the presence of δ -phase can compromise the ductility and corrosion of IN625 welded joints [17] or clad components [18]. Solubilization above 1000 °C in a DED-processed IN625 decreases the presence of δ -phase, and above 1100 °C will entirely remove this phase in wrought IN625 [19]. A previous study [20] explored the effect of SR heat treatment at 900 °C for 1 h and SR + solubilization at 1100 °C–1150 °C. They found that SR led to the hardest condition while the solubilization softened the matrix. Bon et al. [14], using DED-LB, found similar results using SR (800 °C for 1 h) and SR + solubilization (1100 °C for 1 h).

In this work, we aim to develop a three-degree freedom DED-WA (GMAW-RMDTM) equipment to understand the effect of the process fabrication of IN625 components, the impact of heat treatments and orientation of samples on the microstructural features and mechanical properties, specifically tensile and fracture toughness tests. Furthermore, chemical composition, microstructure, and corrosion resistance analyses were carried out in the as-built (AB), stress relief (SR), and SR + solubilization (SR + S) conditions. These results will help better understand the GMAW-RMDTM process for the fabrication of IN625 components by DED-WA. Merging different mechanical and electrochemical attributes allowed the identification of strong, ductile, tough, and corrosion-resistant DED-WA alloys to endure harsh environmental threats.

2 Experimental procedure

This work was divided into three stages. First, we designed and fabricated DED-AW equipment, making a cartesian table with CNC and a welding controller. Second, to cut the specimens, we used the equipment's parameterization and fabrication of rectangular geometries with external dimensions of 210 × 100 × 60 mm and 10 mm thickness walls. Finally, the microstructure, corrosion resistance, and mechanical properties were assessed to identify which alloy presents the most favorable combination of properties. The system DED-AW equipment was divided into three main parts: (i) metallic structure made of ASTM A 513 carbon steel, (ii) three ball screws coupled to a stepper motor with a torque of 15 kgf.cm, and (iii) controller system of the GMAW with regulated metal deposition (RMDTM) [11].

To carry out the feeding and melting of the consumable wire and to enable layer deposition, a Miller PipeWorks 400 welding source was used. In addition, a torch was coupled to the “Z” axis of the equipment to ensure that the layers were deposited without compromising the previous layers and to guide the consumable wire to the

weld pool. The layer deposition was conducted on an ASTM A-516 Gr.70 substrate, selected due to its low cost compared to IN625. Since the first layer suffered high substrate dilution in the weld pool, these layers were discarded during the chemical and mechanical analysis of the samples. The consumable wire used was an AWS SFA 5.14 ERNiCrMo-3, whose chemical composition is similar to the IN625 alloy specified for rod and bar products [21] and powder for additive manufacturing (AM) [22], as depicted in Table 1. To obtain an ideal wall thickness and greater stability during deposition, the diameter of the filler material was defined as 1.2 mm, as also used in previous works [5, 23]. In addition, a 70% argon and 30% helium gas mixture was employed to protect the molten pool upon deposition. Besides preserving the molten pool from oxidation and contaminants, this gas mixture also provides better wettability, granting a better superficial finishing of the deposited layers [24].

The deposition parameters were selected from single beads-on-plate depositions until the best relationship between layer profile and penetration was reached.

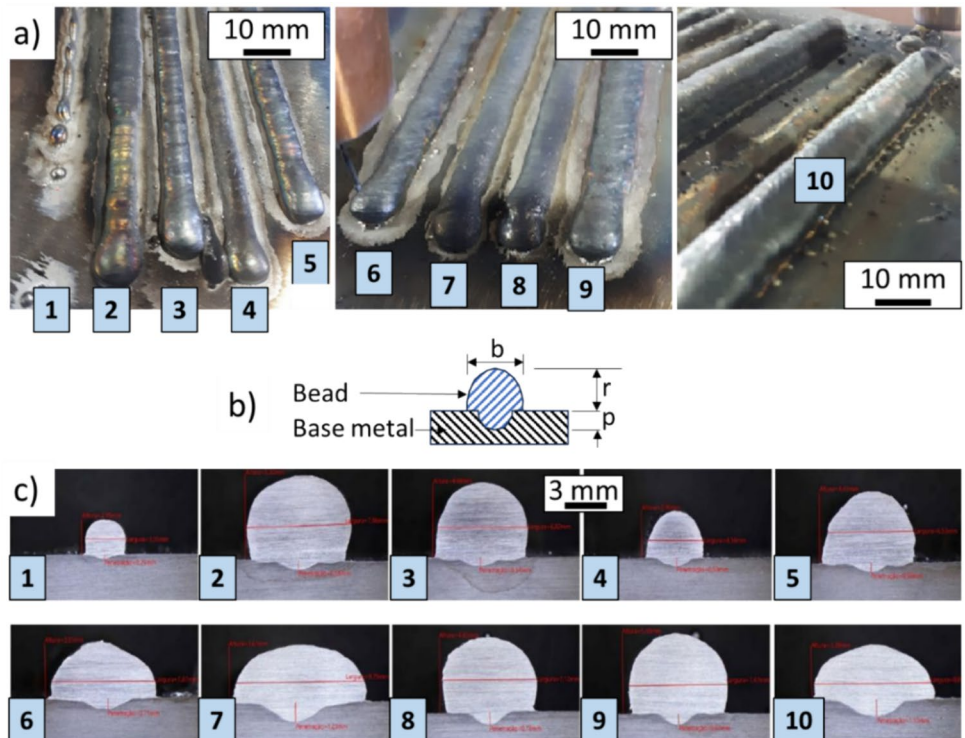
Bead-on-plate single passes were used to conduct the parametrization. The current, voltage, scan speed, feed rate, and heat input were varied between 113–148 A, 12.9–14.6 V, 7–13 mm/s, 5.3–6.5 mm/s, and 163–219 J/mm, respectively. To fabricate the walls, a rectangular shape with 210×100×60 mm and 10 mm thickness walls was selected, as shown in Fig. 1, to allow a better heat distribution during the deposition. Given the high thermal gradient during the deposition of the layers, temperature monitoring was conducted with a Type K thermocouple to remain below 400 °C. This type of control is critical for controlling and avoiding the formation of deleterious phases and precipitates [25, 26].

Table 2 presents the parameters for depositing ten beads considered for process parametrization. Figure 1 shows the bed on plate single passes, a schematic view of a cross-section of the passes depicting the penetration depth (*p*), bead width (*b*), reinforcement height (*r*), and the cross-section of the ten assessed single passes. A key parameter controlled during the deposition of the layers was the heat input (*H*) given in J/mm, which is defined by $H = V \cdot I / v$,

Table 1 Experimental chemical composition (wt %) of the welding wire and comparison with the ASTM F446-23 and F3056-14 (2021)

Material	Ni	Cr	Mo	Si	Fe	Mn	Al	Ti	Cu	Nb+Ta
Wire	Bal	21.80	8.70	0.04	0.03	0.02	0.09	0.18	0.01	3.60
ASTM F3056-14 (2021)	Bal	20.00–23.00	8.00–10.00	0.50 max	5.00 max	0.50 max	0.40 max	0.40 max	–	Nb 3.15–4.15
ASTM B446-23	58.00 min	20.00–23.00	8.00–10.00	0.50 max	5.00 max	0.50 max	0.40 max	0.40 max	–	3.15–4.15

Fig. 1 Bead-on-plate single passes for parametrization of the ten conditions assessed, **a** visual aspect of the deposited passes, **b** schematic view of the cross-section of a single bead, and **c** cross-section of bead passes; *p*, *b*, and *r* stand for penetration depth, bead width, and reinforcement height, respectively



where V is the voltage (V), I is the current (A), and v is the travel speed (mm/s). The combination of parameters with high current and high travel speeds presented the lowest heat input. These conditions delivered irregular passes with shallow penetration (conditions 1–5)—Increasing the heat input increased the penetration depth and bead width. Hence, the selected process parameters for the depositions correspond to those from conditions 7 and 10, where the highest build quality is for current of 113 and 117 A, voltage values of 12.9 and 13.1 V, transverse speed of 7 mm/s, feed speed of 5.3, and heat input between 208 and 219 J/mm.

Figure 2 shows the rectangular component fabricated by DED-AW. According to the selected parameters to manufacture this part, the voltage was around 13 V, the

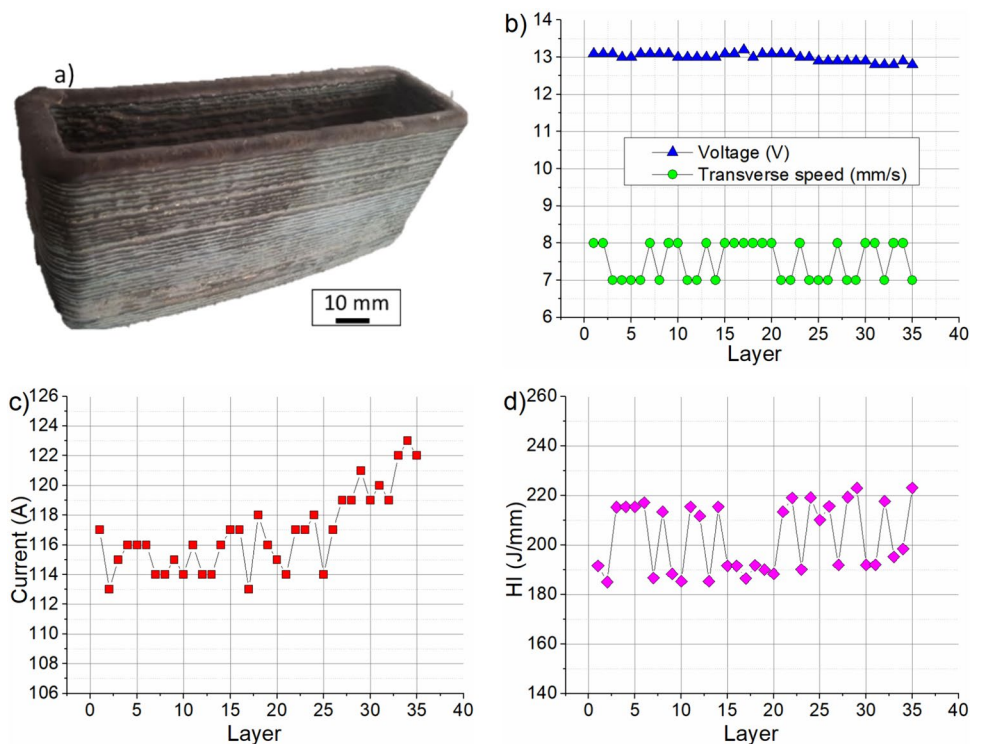
transverse velocity varied between 7 and 8 mm/s, the current varied between the first layers until layer number 26, between 112 and 118 A, and then increased until 123 A in the latest layers. Finally, the heat input was kept constant around 182 to 222 J/mm with an average value of 202 J/mm. Therefore, the parameters were observed within the established parametrization.

To analyze the influence of heat treatments, three conditions were considered: (i) as-built (AB) without heat treatment; (ii) a stress relief (SR) up to 800 °C for 1 h, and (iii) SR + solubilization heat treatment (SR + S) at 1150 °C for 1 h. The heat treatments were based on previous works [15, 19, 20]. The heating rate was 200 °C/h, and the cooling rate for SR was the same up to 200 °C, and then the cooling

Table 2 Parameters used to establish the best fabrication conditions based on the bead-on-plate single passes shown in Fig. 1, where the current (I), voltage (V), transverse speed (v), and feed rate (g) were changed

Sample	I (A)	V (V)	v (mm/s)	g (mm/s)	H (J/mm)	p (mm)	b (mm)	r (mm)	Macro defects
1	148	14.6	11	6.5	196	0.29	3.05	2.19	Free
2	145	14.6	13	6.5	163	0.59	7.96	5.32	Free
3	138	14.2	12	6.3	163	0.54	6.82	4.68	Free
4	135	13.9	9	6.0	209	0.53	4.16	2.96	Free
5	136	13.9	9	6.0	210	0.58	6.53	4.43	Free
6	117	13.1	8	5.3	192	0.71	7.87	3.51	Free
7	117	13.1	7	5.3	219	1.23	10.17	6.61	Free
8	129	13.1	9	5.7	188	0.78	7.12	4.65	Free
9	130	12.9	8	5.8	210	0.67	7.47	5.00	Free
10	113	12.9	7	5.3	208	1.10	9.79	3.39	Free

Fig. 2 a Component fabricated by DED-AW and the welding parameters during the 35 layers' depositions, b transverse speed and voltage, c current, and d heat input (HI)



continued out of the furnace. However, after solubilization, water cooling was used to reach room temperature.

Samples were analyzed in three distinct regions of the deposited specimens to evaluate homogeneity: top (T), middle (M), and bottom (B), as seen in Fig. 3. For chemical analysis, the samples of the deposited material were analyzed through optical emission spectrometry using a SPECTROMAXx. A Panalytical–Empyrean X-ray diffractometer with a copper tube was used for the different phases' peak positions. Hardness tests (Vickers) were conducted in microdurometer Leica, VMHT MOT, in the B, M, and T samples using loads of 300 g during 15 s. To reveal the microstructure, the metallographic prepared surfaces were etched with aqua regia (hydrochloric acid: nitric acid: acetic acid in = 1: 1: 1 volume) [27]. Light optical microscopy was utilized to evaluate the different microstructures obtained in all sample regions and for various heat treatments. In addition, scanning

electron microscopy (SEM) was also used to assess the microstructure before (Thermo Fisher Scientific Quanta 650 FEG) and after electrochemical testing (Thermo Fisher Scientific Quanta FEI Quanta 400). The EDS interaction volume was calculated using Casino V2.42 software [28]. Thermo-Calc, with Nickel-based superalloys database (TCNI12, MOBNI6), was used to determine the volume fraction of phases in equilibrium at 800 °C and 1100 °C.

To evaluate the mechanical properties of the manufactured parts, specimens were cut in the vertical direction (transverse of the deposition direction), and horizontal direction (parallel to the deposition direction), and tensile tests were conducted under displacement control at a displacement rate of 2 mm/min, according to the ASTM E8-24. For tensile testing, samples were machined according to Fig. 3. Crack tip opening displacement (CTOD) tests were conducted according to ASTM E1820-24 in single-edge-notched bend—SE(B)—samples loaded in three-point

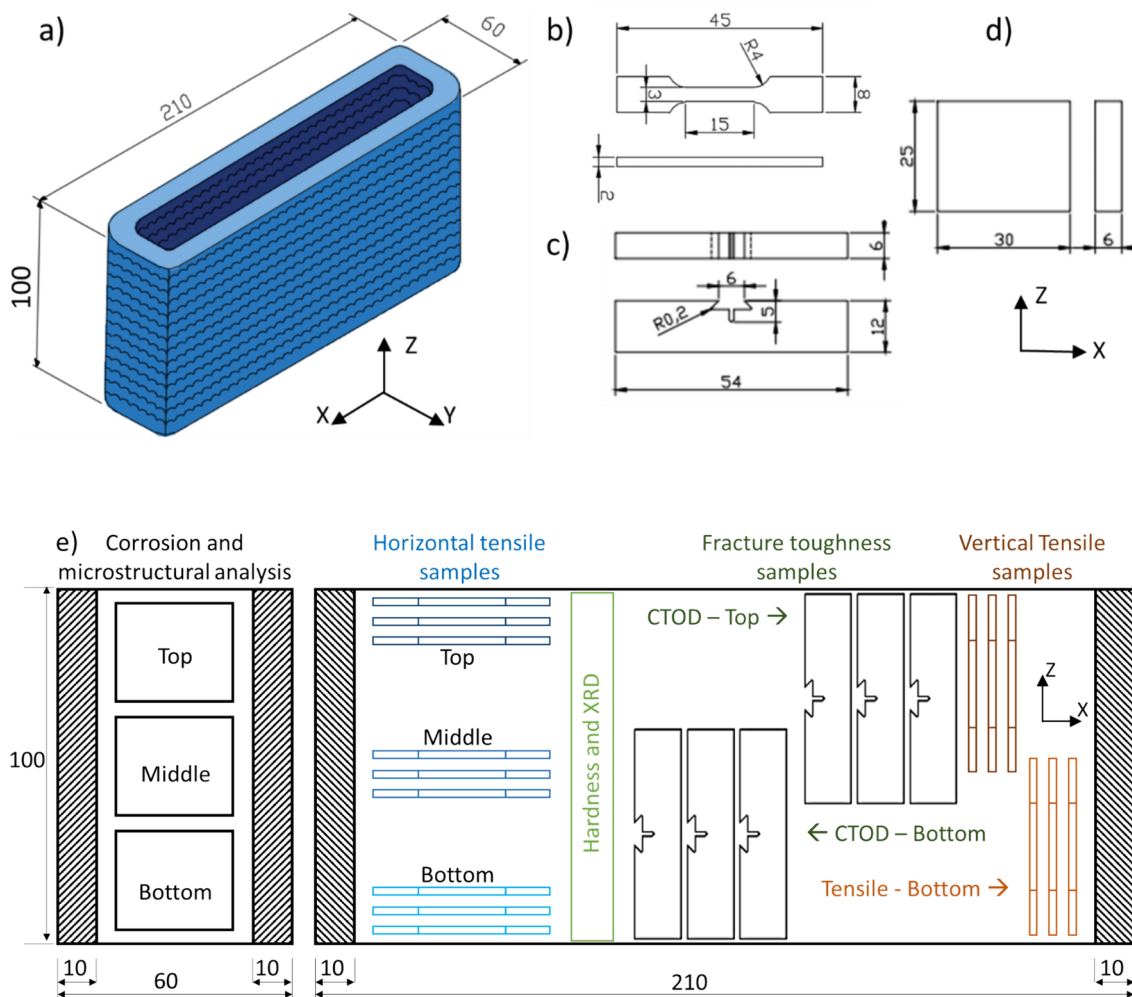


Fig. 3 Rectangular geometry fabrication in **a**, tensile samples in **b**, fracture toughness samples in **c**, corrosion samples in **d**, and schematic distribution of samples in one of the faces of the rectangular geometry in **e**. Dimensions in mm

bending. Samples were ground and polished to a mirror-like condition to observe crack growth during fatigue precracking before CTOD tests. CTOD tests were conducted with an increasing load and crosshead rate of 1 mm/min at 25 °C. A 100 kN MTS Landmark N servo-hydraulic machine was used to conduct the tensile tests, the precracking of the fracture toughness tests, and their corresponding tests. Toughness values for this material correspond to the onset of unstable crack extension, depicted in the ASTM E1820-24 standard as $CTOD_{Ic}$ and J_{Ic} . Due to the thin thickness and high plasticity of the IN625, toughness values near the onset of slow, stable crack extension ($CTOD_{Ic}$ and J_{Ic}) were not determined in this work.

Electrochemical analyses were also employed using a conventional three-electrode cell set-up consisting of a platinum mesh counter electrode and a saturated calomel reference electrode (SCE). A Gamry 600 + potentiostat was used for all electrochemical tests. The working electrodes were ground to a 1500 grit SiC finish, being tested in the following conditions: (i) as-built (AB) without heat treatment; (ii) a stress relief (SR) up to 800 °C for 1 h, and (iii) SR + solubilization heat treatment (SR + S) at 1150 °C for 1 h. Again, the top (T), middle (M), and bottom (B) regions were evaluated. Wrought IN625 and the consumable wire AWS SFA 5.14 ERNiCrMo-3 were included for comparison purposes and used as a benchmark.

Demineralized water and high-purity reagents (> 99%) were used to prepare substitute ocean water according to ASTM D1141-98 (2021), containing inorganic salts in proportions and concentrations representative of ocean water. All the electrochemical experiments were conducted in open air at 25 ± 2 °C. The working electrode, with an exposed area of 0.4 cm², was left for 1 h at an open circuit, which allowed the stabilization of the open circuit potential (OCP) before polarization tests were conducted. Potentiodynamic polarization was performed at -300 mV vs OCP, and potential swept upwards at a scan rate of 1 mV/s until a current density of 10 mA cm⁻² was reached. The corrosion current density (i_{corr}) was estimated by extrapolating the cathodic ‘Tafel-like’ region since it resulted in about a decade of linearity. Other parameters, such as the current density associated with the passive window and the transpassivation potential (E_{transp}), were also assessed from the polarization curves. E_{transp} was utilized as an index to potentials above which passive currents were exceeded. In the case of pitting corrosion, the term E_{pit} is used instead. E_{transp} and E_{pit} are often used interchangeably in cases where testing is at a temperature that exceeds the critical pitting temperature of the alloys being studied. In this study, the E_{transp} is most suitable for the alloys tested and the terminology used hereafter.

Electrochemical impedance spectroscopy (EIS) was performed following 1 h of immersion at OCP using

$\Delta E = 10$ mV_{rms}. A frequency range of 10^5 to 10^{-2} Hz was considered, recording 10 points per decade. In addition, the Measurement Model Program published by Watson and Orazem [29] was used to analyze the impedance data based on the linear regression approach. Besides indicating the error structure of EIS measurement [30], the Measurement Model regression is functional, estimating the polarization and ohmic resistances and extracting system capacitive-like responses [31], showing distributed-time-constant behavior that obscures the value of the capacitance. This approach has been successfully employed to model the experimental EIS data of additive-manufactured alloys, such as laser-beam-melted (LBM) 17-4PH martensitic stainless steels [31].

Regressing a representative model with impedance $Z(\omega)_{model}$ to $Z(\omega)_{exp}$ allows obtaining essential parameters containing information on resistive and capacitive properties of the interface. The model is an ohmic resistance, R_w , arranged in series with a certain number of Voigt elements, each composed by a resistor R in parallel with a capacitor C , $Z_C(\omega) = -j(\omega C)^{-1}$, resulting in a general structure of Eq. 1: $\tau_i = R_i \bullet C_i$ is the time constant of the i -th Voigt element, each with a capacitance given by $C_i = \tau_i/R_i$.

$$Z(\omega) = R_e + \sum_i \frac{R_i}{1 + j\omega\tau_i} \quad (1)$$

The Voigt Measurement model regressing assists in extracting the electrolyte and the polarization resistances and the overall effective capacitance of the surface, C_{eff} , from the experimental impedance data [42]. High frequencies induce the impedance of the i -th Voigt element approaching the impedance of its capacitive component, and Eq. 1 results in:

$$Z(\omega) = R_e - j\omega^{-1} \sum_i (C_i)^{-1} \quad (2)$$

The second *rhs* term of Eq. 2 isolates the capacitive contributions:

$$C_{eff}^{-1} = \sum_i (C_i)^{-1} \quad (3)$$

When frequencies tend to zero, the impedance of the i -th Voigt element reduces to its resistance component, and the polarization resistance, R_p , can also be obtained from Eq. 1

$$R_p = Z_{\omega \rightarrow 0}(\omega) - R_e = \sum_i R_i \quad (4)$$

To further evaluate the corrosion resistance, the ASTM G48-11(2020) standard using method A, was employed to analyze the samples' surface stability. The samples' surfaces

were finished with 120-grit abrasive paper. During testing, samples with dimensions approximately $30 \times 18 \times 8 \text{ mm}^3$ were immersed in 600 ml of ferritic chloride electrolyte for 72 h at 50 °C. The surface was checked, and the weight loss was measured.

3 Results

3.1 Microstructural characterization

Figure 4a shows the chemical composition measured in the as-built condition in the top (T), middle (M), and bottom (B) locations, as well as the hardness profiles of the deposited and heat-treated samples. The chemical composition is similar between the different heights and fulfills the requirements of ASTM F3056-14 (2021). However, some Fe contamination was detected

at the bottom due to the incorporation of the substrate. Table 3 shows the phase volume percentage calculated using Thermo-Calc. According to the small changes in chemical composition between three different heights, the presence of γ -Ni, δ (Ni_3Nb), and σ present similar volume percentages. The bottom region presents the only difference with a little increase in the δ and σ due to the iron contamination. Figure 4b exhibits the diffractograms of all conditions where only the γ -Ni phase is indexed, without evidence of δ . In Fig. 4d, the Vickers scale's hardness is similar within the three measured positions. Hardness in the SR condition delivered the highest values, followed by the AB and SR + S conditions. This means some products have precipitated in the SR treatment, yet in low quantity to be detected by laboratory X-ray diffractometer (XRD). In contrast, in the SR + S condition, these precipitated products might be solubilized in the matrix, as calculated by Thermo-Calc.

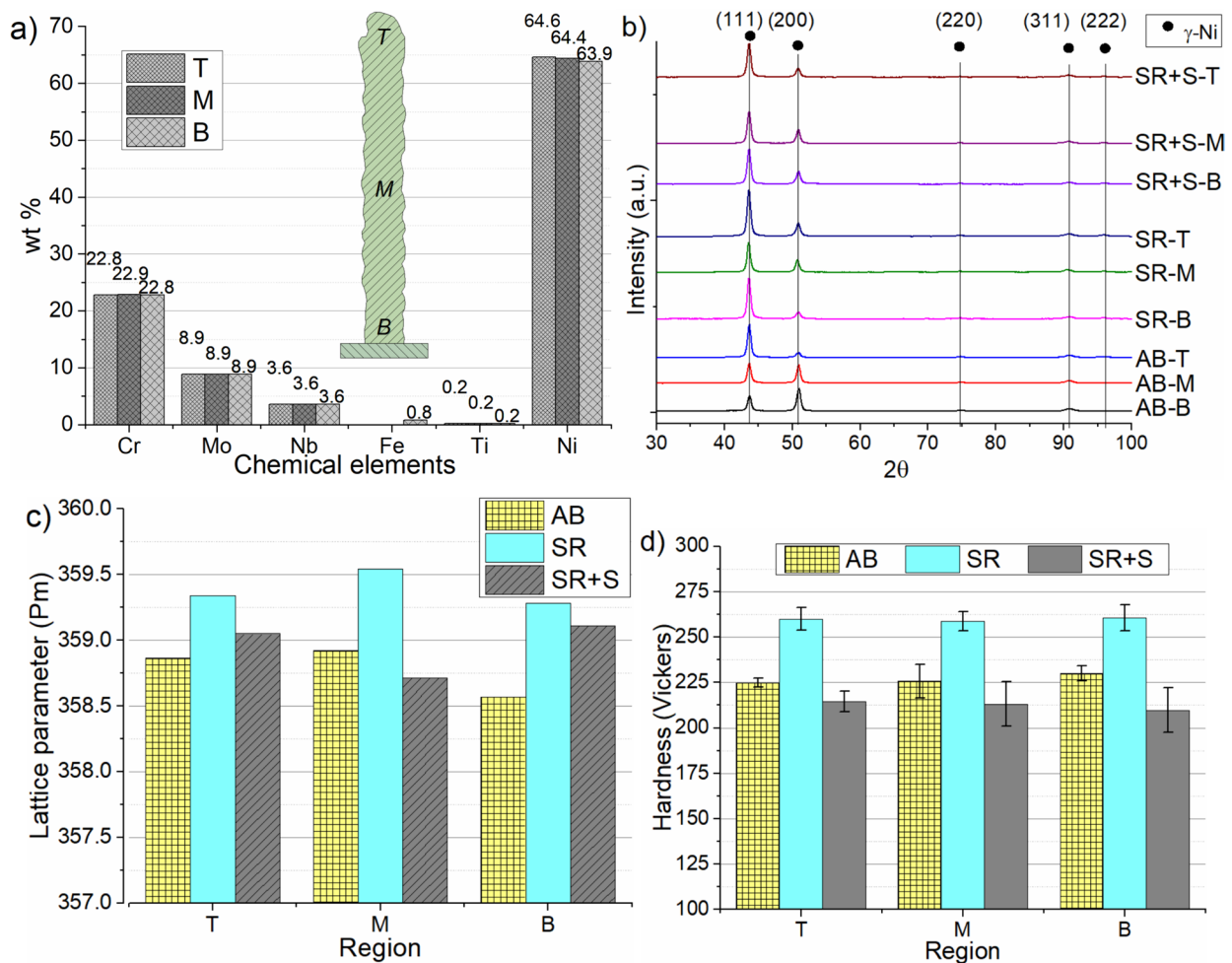


Fig. 4 a Experimental chemical composition measured in the as-built (AB) sample in the top (T, 80 mm), middle (M, 45 mm), and bottom (B, 7 mm), considering the substrate material as a zero, b x-ray

diffractograms, c lattice parameter and, c average Vickers hardness of the as-built and heat-treated samples, such as the stress relief (SR) and stress relief followed by solubilization (SR + S)

Table 3 Phase volume percentage calculated under equilibrium using Thermo-Calc

Position	Temperature (°C)	Phases volume percentage		
		γ -Ni	Ni ₃ Nb	σ
Top, Middle, and Bottom	800	82.66 – 83.36	7.89 – 7.96	8.75 – 9.38
	1100	100		

According to Fig. 4c, the lattice parameter increases in the SR condition, meaning the formation of precipitates, while the SR + S experienced the solubilization of some precipitates' solubilization, which follows the trend shown by the hardness.

Figure 5 depicts the macro view of the cross-section in the horizontal disposition in the first row, the microstructure in the second row, and higher magnification photos in the third row. In the macro images, no defects were observed. However, the wavy surface caused by the layers' deposition is noticed. Figure 5a–b display similar columnar products that change their format from one melt pool to another. This means the SR heat treatment does not alter the microstructure significantly but precipitates some phases, most likely the δ phase, which increases the mechanical strength at the expense of ductility [15]. After solubilization, as shown in Fig. 5b, the microstructure changed significantly, and the columnar microstructure is less evident than in the other conditions—however, homogenization occurred. Thus, etching concentrates on the grain boundaries instead of the columnar grain boundaries.

Figure 6 results from a more detailed characterization using the electron microscope with the backscattering (BSE) and energy-dispersive X-ray Spectroscopy (EDS) detectors. In low magnification (Fig. 6a, d, and g), can be seen some micropores ($< 5 \mu\text{m}$) indicated by black arrows. These pores originated during the fabrication process.

Table 4 shows the approximate chemical composition measured by EDS. Be aware of the limitation of using this technique once its interaction volume for 15 keV is about $0.5 \times 0.5 \times 0.5 \mu\text{m}^3$, which can result in a mixed result of other regions. Using the BSE detector made it possible to see areas that appeared brighter than the matrix. This corresponds to Nb enrichment zones and Nb-rich Laves phases that belong to the cell's boundaries originated by the rapid cooling [32, 33]. These results are depicted in the AB and SR conditions (Fig. 6a–b and d–e); however, the SR + S (Fig. 6g–h) was able to solubilize these enriched zones. Spots measured by EDS-1–2, EDS 6, and 8 show these differences in chemical composition.

At intermediated and high magnification, it is possible to see that Nb and Mo-enriched zones at the AB and SR are zones where different phases are allocated, such as MC-type carbides, δ phase, and Laves phase (Fig. 6b–c and e–f). On the other hand, the SR + S does not evidence δ or Laves.

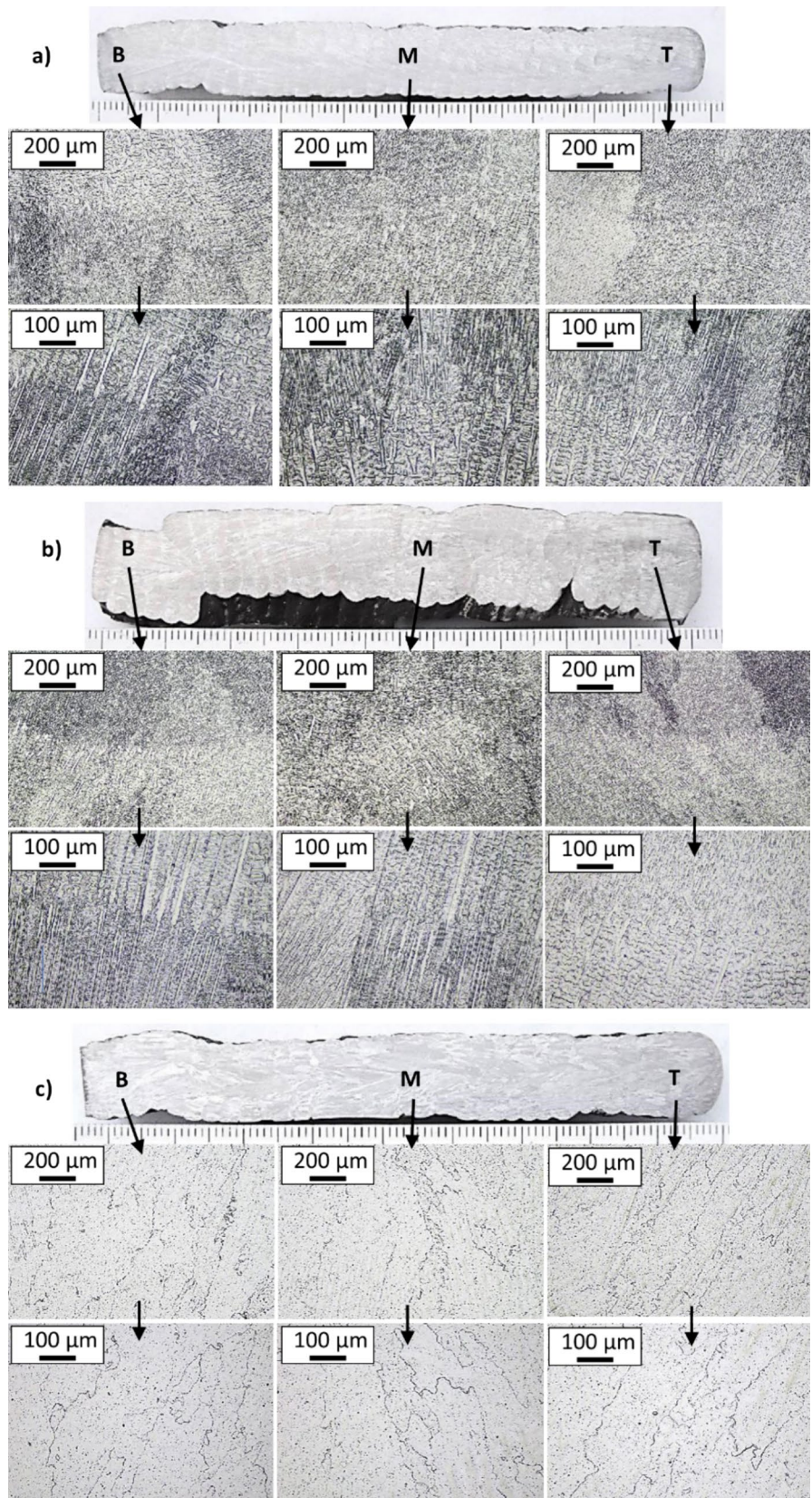
3.2 Mechanical strength and fracture toughness

Figures 6 and 7 depict the mechanical properties results of the tested samples in all three conditions, namely as built (AB), stress relief (SR), and stress relief plus solubilization (SR + S). In Fig. 6, tensile test results of the three repeats, in horizontal and vertical orientations, are shown. For the horizontal samples, the elongation at fracture behavior was similar in all three conditions, with a slight decrease in elongation for the top horizontal sample. Vertical-oriented samples displayed identical behavior, except for the SR + S condition, which presented the highest elongation at fracture, approaching 50%, as seen in Fig. 6a. Yield strength results, Fig. 6b, show that the SR condition has the highest value, with almost 500 MPa for all orientations; in addition, all orientations presented similar results, with the SR condition showing the highest values when compared to SR + S and AB conditions. Tensile strength results can be seen in Fig. 6c. It can be noted that the SR condition presented the highest values of tensile strength, in some cases extending above 800 MPa. Due to the significant elongation to fracture, the tensile samples' fracture surface reveals a ductile surface fracture that evidences the microvoids' coalescence in all conditions; however, this type of fracture is typical of such conditions, and images were not added to seek clarity in the core of the work.

Regarding orientations, horizontal samples showed slightly higher values than vertical samples for all conditions. In short, the SR condition presented the highest mechanical improvements at the expense of elongation at fracture. At the same time, orientations are similar, with slightly higher results for the horizontal samples, except for elongation at fracture. Yet, this behavior has been reported in DED-WA samples of the same material [10].

Figure 8 shows the fracture toughness results. Figure 8a shows the typical force vs. crack mouth opening displacement (F vs. CMOD), depicting shorter curves for the SR condition than the AB and SR + S. Analytically, toughness can be related to the area of the curve, representing the energy accumulated until the highest value of force. Hence, less area corresponds to less toughness. Figure 8a illustrates the average and error bar for each condition. In this case, the samples that presented the more ductile behaviors and less hardness, SR + S followed by AB, presented the best toughness with CTOD average values close to 1.5 mm. In comparison, the SR presented toughness

Fig. 5 Macro and microstructures of the studied conditions showing the cross-section of the walls in a horizontal disposition: **a** AB, **b** SR, and **c** SR+S. The first column depicts a macro image, the second column shows photos with low magnification, and the third row presents images with high magnification



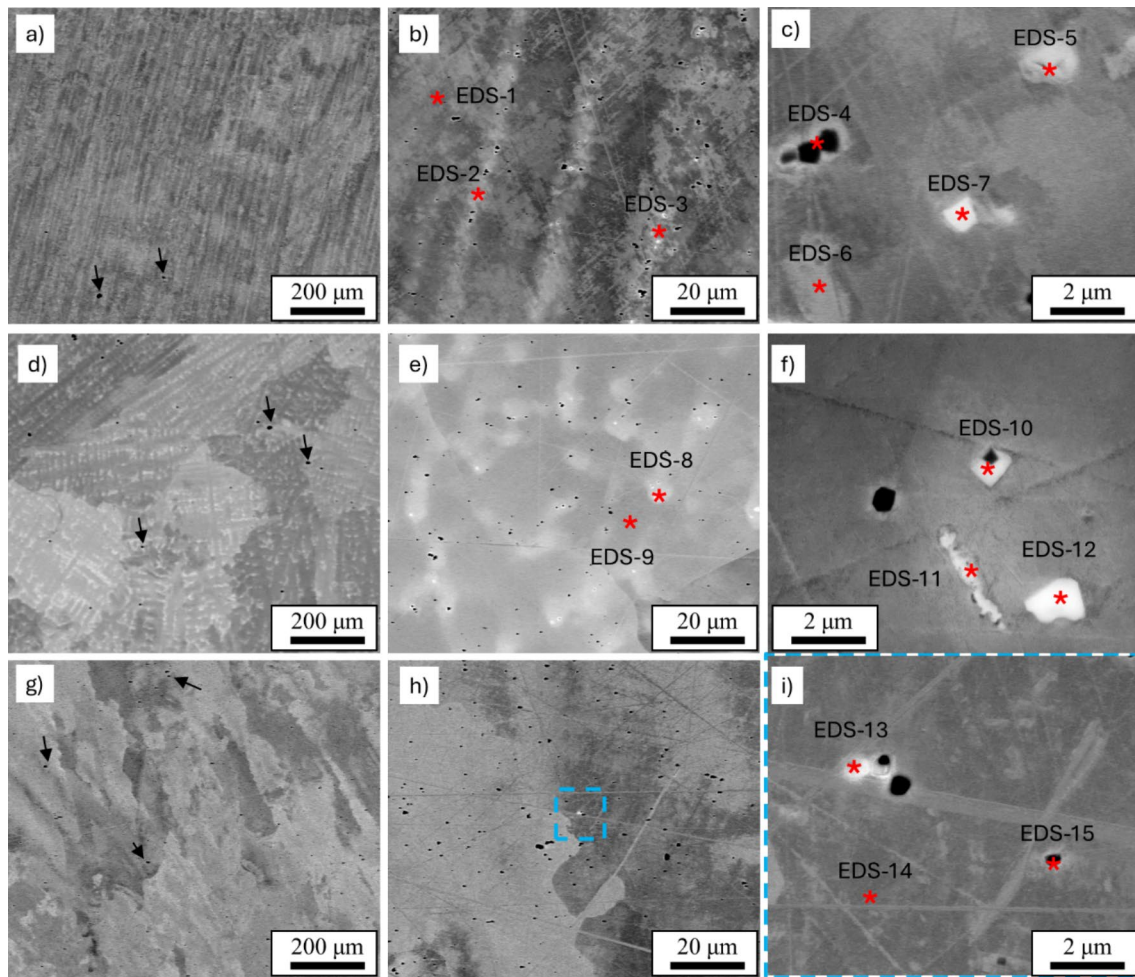


Fig. 6 Microstructural analysis of all conditions: AB (a–c), SR (d–f) and SR+S (g–i). Some spots have their chemical composition measured by EDS, and these results are in Table 4. Images were taken with a BSE detector

Table 4 Chemical composition (wt %) of the EDS spots. The chemical composition measured in Fig. 4 (AB*) has been added for comparison purposes, and phases have been matched according to the reference [34]

Sample	Spot	Ti	Cr	Ni	Nb	Mo	Possible phase
AB	EDS-1		22.5	64.8	3.5	9.2	Matrix γ -Ni
	EDS-2		21.0	60.6	6.9	11.6	Matrix γ -Ni with Nb and Mo enrichment
	EDS-3		19.7	57.7	12.2	10.4	Laves
	EDS-4	32.3	8.9	13.9	40.7	3.3	MC
	EDS-5	3.5	5.8	10.8	76.4	3.6	δ
	EDS-6		21.6	60.8	6.7	10.9	Matrix γ -Ni with Nb and Mo enrichment
SR	EDS-7	1.2	6.0	12.7	75.1	5.0	δ
	EDS-8		21.4	60.5	7.3	10.8	Matrix γ -Ni with Nb and Mo enrichment
	EDS-9		22.8	64.1	3.6	9.5	Matrix γ -Ni
	EDS-10	3.3	9.0	18.7	63.6	5.3	δ
	EDS-11		17.4	47.1	19.1	16.5	Laves
	EDS-12	3.4	4.5	8.5	80.5	3.1	δ
SR+S	EDS-13	4.0	8.3	16.9	66.7	4.1	MC + matrix γ -Ni
	EDS-14		22.4	63.6	4.2	9.8	Matrix γ -Ni
	EDS-15	9.6	20.1	48.9	13.5	7.9	MC
AB*		0.2	22.8	64.6	3.6	8.9	Matrix γ -Ni

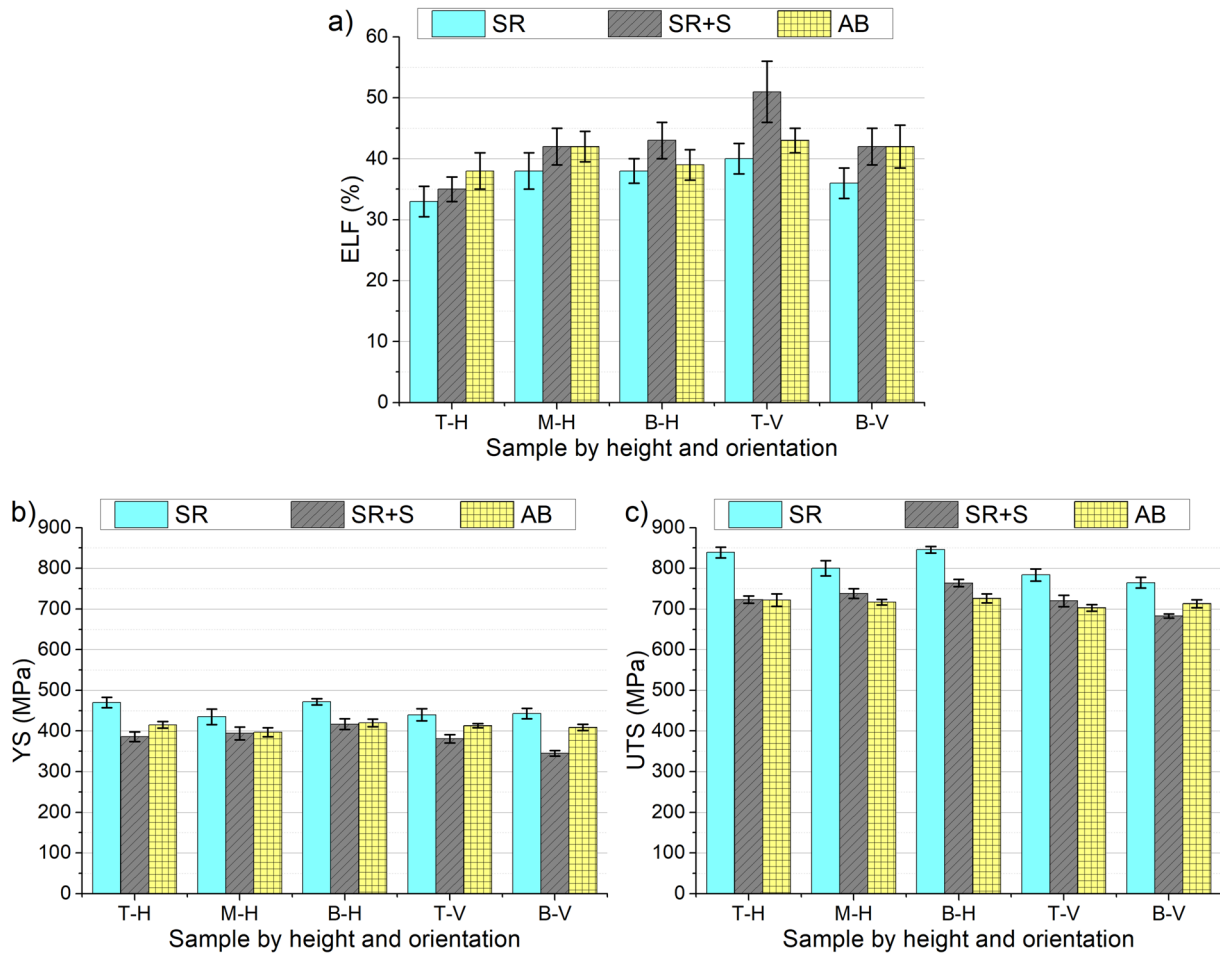


Fig. 7 Mechanical strength and elongation at fracture of samples. **a** Elongation at fracture (ELF, %), **b** Yield strength (YS, MPa), and **c** Ultimate Tensile strength (UTS, MPa). All graphs show the as-built

and heat-treated conditions (AB, SR, and SR+S). Samples were taken from the top (T), middle (M), and bottom (B) in the vertical (V) and horizontal (H) orientations

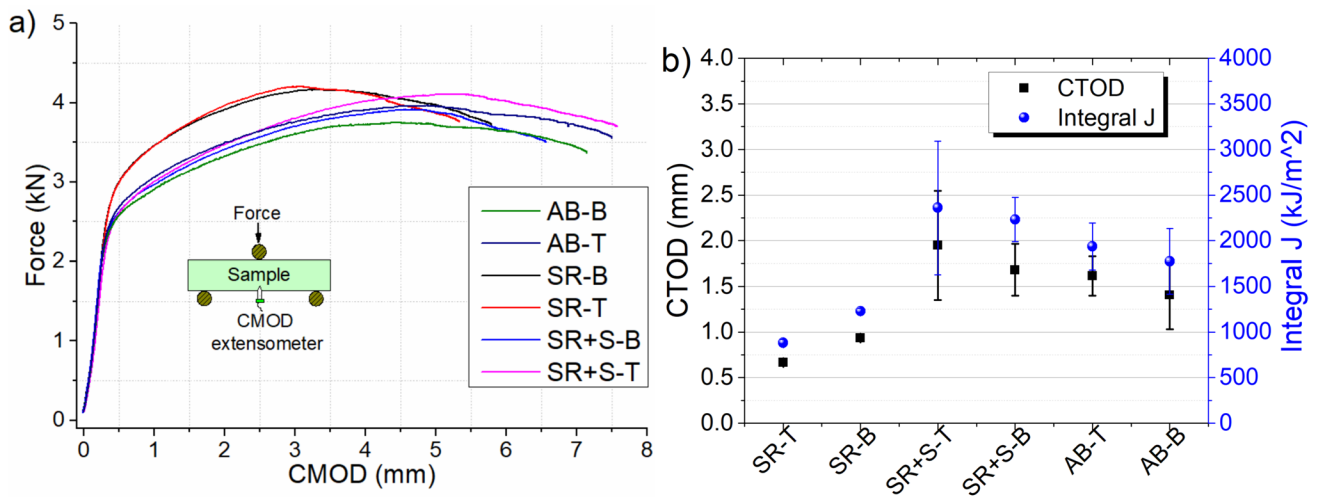


Fig. 8 Fracture toughness summary results: **a** F vs CMOD representative curves of the fracture toughness test and **b** average CTOD and integral-J values in each assessed condition

values below 1.0 mm—CTOD samples with notches parallel to the layers. Additionally, the J integral values have been added for comparison purposes; however, they represent the trend described by the CTOD parameter.

Figure 9 shows the fracture surface of the fracture toughness samples where part a) represents schematically the different regions within the samples and b) the real fracture surfaces. The pre-crack size average was 8.4 mm (0.7 W), which follows the E1820-24 standard, between 0.45 W and 0.70 W for J and δ determination. The crack size at region 2 depicts an average of 2.6 mm, similar for all conditions, reflecting its high capacity to resist crack propagation. An interesting observation is that region 2 of the SR condition is smoother than other conditions, showing that the propagation in the AB and SR + S suffer a more tortoise path, therefore expending more energy to propagate the cracks.

3.3 Corrosion assessment

The polarization curves are exhibited in Fig. 10. All curves displayed a clear passivation plateau upon anodic polarization associated with restricted current density values below $5 \times 10^{-6} \text{ A cm}^{-2}$. Similar polarization curves have been observed in WAAM-produced Inconel 625 immersed in a 3.5% NaCl solution [10, 35], which closely resembles the salinity of the synthetic seawater employed in this study. A steep increase of current density occurs only for high polarization, being the passivation stability between 500 and 800 mV ($E_{transp} - E_{corr}$), and the corrosion current density, i_{corr} , values low, in the order of $10^{-6} \text{ A cm}^{-2}$ regardless of the condition (AB, SR, SR+S) and the region evaluated (Top, Fig. 10a, Middle, Fig. 10b, Base, Fig. 10c). However, compared to the wire, the DED-WA alloys displayed, irrespective of the condition, a lower current density upon anodic polarization for a comparable extent of polarization, indicating the superior corrosion resistance of DED-WA alloys in substitutive seawater, as highlighted by the insets in Fig. 10a–c indicating the

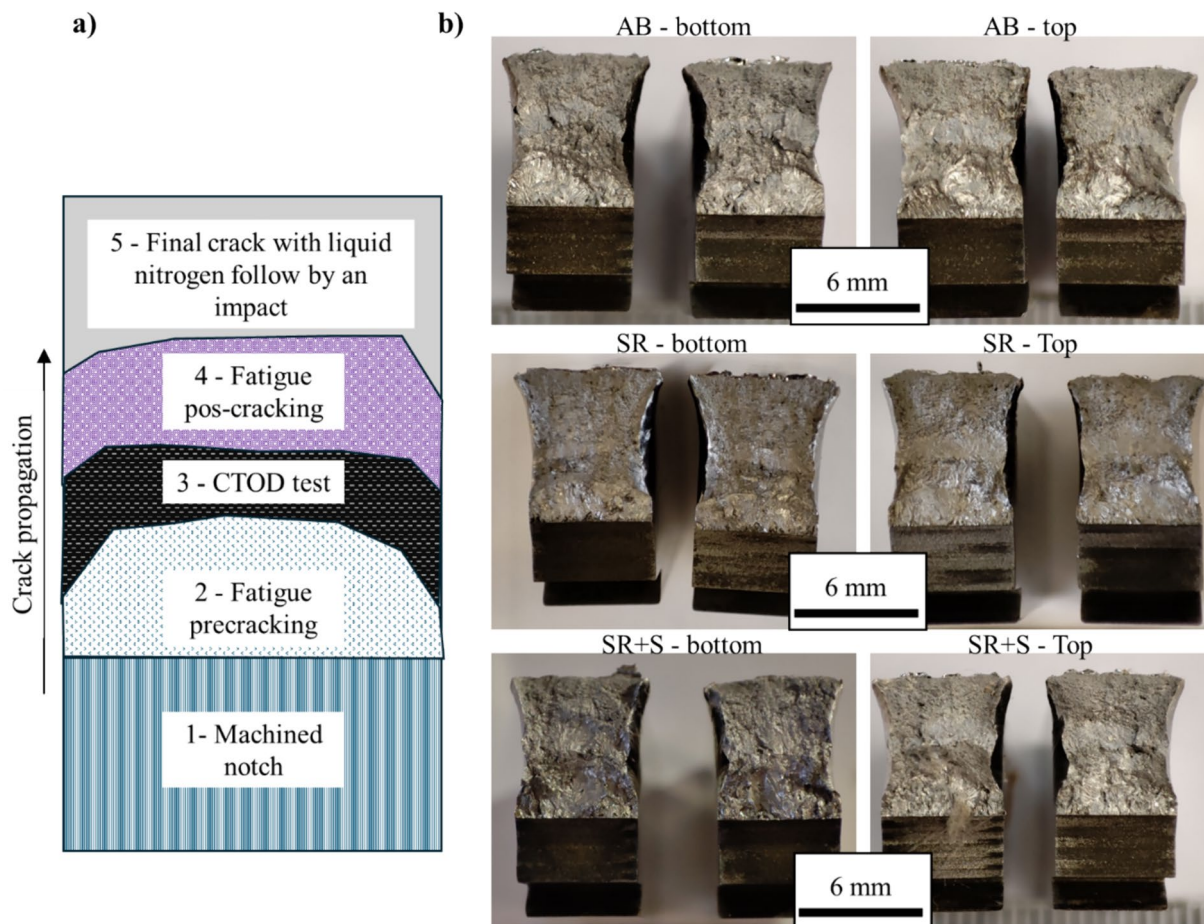


Fig. 9 The typical fracture surface of the fracture toughness samples for each condition: **a** shows the schematic view of the different zones during the crack propagation and **b** the halves of representative surface fractures

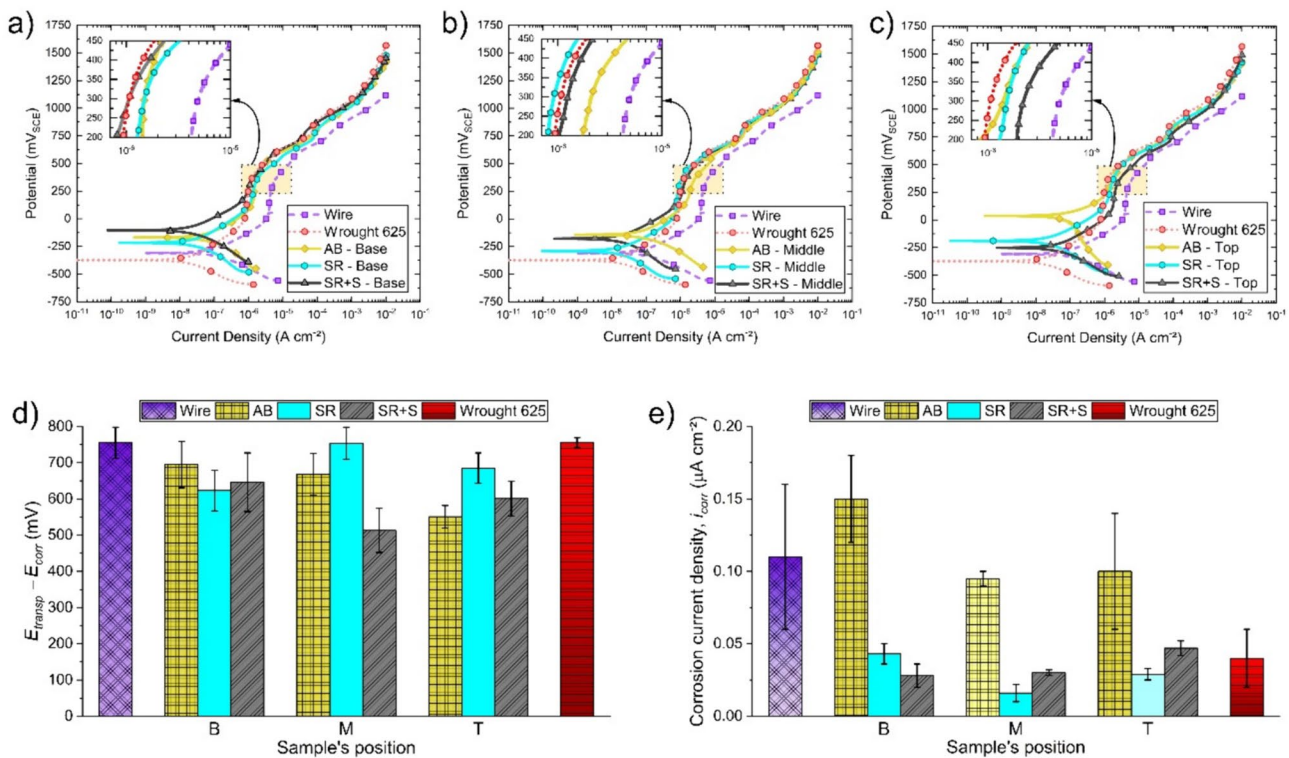


Fig. 10 Characteristic potentiodynamic polarization curves of IN625 samples from the **a** base, **b** middle, and **c** top regions of DED-WA-processed specimen at AB, SR, and SR+S conditions. Results of commercially available wrought IN625 and ErNiCrMo-3 wire used for DED manufacturing are compared—inset: zoomed view of the passive region formed upon anodic polarization, which is the range of the passive current density. **d** Difference between the transpassivation

potential, E_{transp} , and the corrosion potential, E_{corr} , indicating the range where the current density is restricted to low levels. **e** Corrosion current density, i_{corr} , values determined around E_{corr} from the Tafel extrapolation of the cathodic branch, which exhibits ‘Tafel-like’ behavior in at least one decade of current from potentials relatively far from E_{corr}

passivation current densities. Concerning the commercial wrought 625 alloys considered as reference, albeit slightly inferior, the DED-WA alloys displayed a similar corrosion current density at the passivation plateau and a comparable potential beyond which a steep increase of current density occurs. These results suggest that the wrought IN625 alloys and those processed by DED-WA displayed a comparable corrosion behavior in seawater, superior to the ErNiCrMo-3 consumable wire to build the DED-WA samples. Taking the corrosion current density, i_{corr} , as an index, the SR and SR+S conditions presented comparable values, which are lower than that offered by the AB alloy state and close to the behavior found for the wrought IN625.

Impedance data and fitting curves from the Measurement Model approach are presented in Fig. 11a–f, from regression, considered the impedance of the analog illustrated in Fig. 11g, being the results from data treatment compiled in Fig. 11h,i. All Nyquist plots, Fig. 11a–c, are characterized by a truncated and enlarged semicircle typical of highly passivated alloys, such as IN625 [36]. Bode plots, Fig. 11d–f, indicate high values of impedance modulus at

the lowest frequency ($|Z|_{f_{req}} = 10^{-2}$ Hz) in the order of $10^5 \Omega \text{ cm}^2$, being the lowest for the wire sample. Bode phase plots indicated a single but enlarged relaxation process in an extended frequency range, indicating superimposed responses related to RC responses, which are typical also of highly passivated alloys [36]. Indeed, irrespective of the location of (Base, Fig. 11a, Middle, Fig. 11b, Top, Fig. 11c), the alloys at AB, SR, and SR+S conditions displayed high polarization resistance, R_p , superior to $700 \text{ k}\Omega \text{ cm}^2$, and as high as $\sim 2000 \text{ k}\Omega \text{ cm}^2$, together with low effective capacitance values, C_{eff} , in the order of 10^{-6} F/cm^2 , characteristic of passive film formation [37]. Interestingly, all the alloys presented superior R_p and lower C_{eff} compared to the wire precursor, and the SR and SR+S conditions displayed similar values to wrought 625 alloys. Among the alloy conditions, the AB alloy displayed the lowest values of R_p and highest values of C_{eff} , indicating the poorest resistance to corrosion in synthetic seawater, whereas the SR and SR+S presented comparable high values.

Figure 12 presents the surface of the alloys after the polarization resistance in Fig. 10. Even after extensive

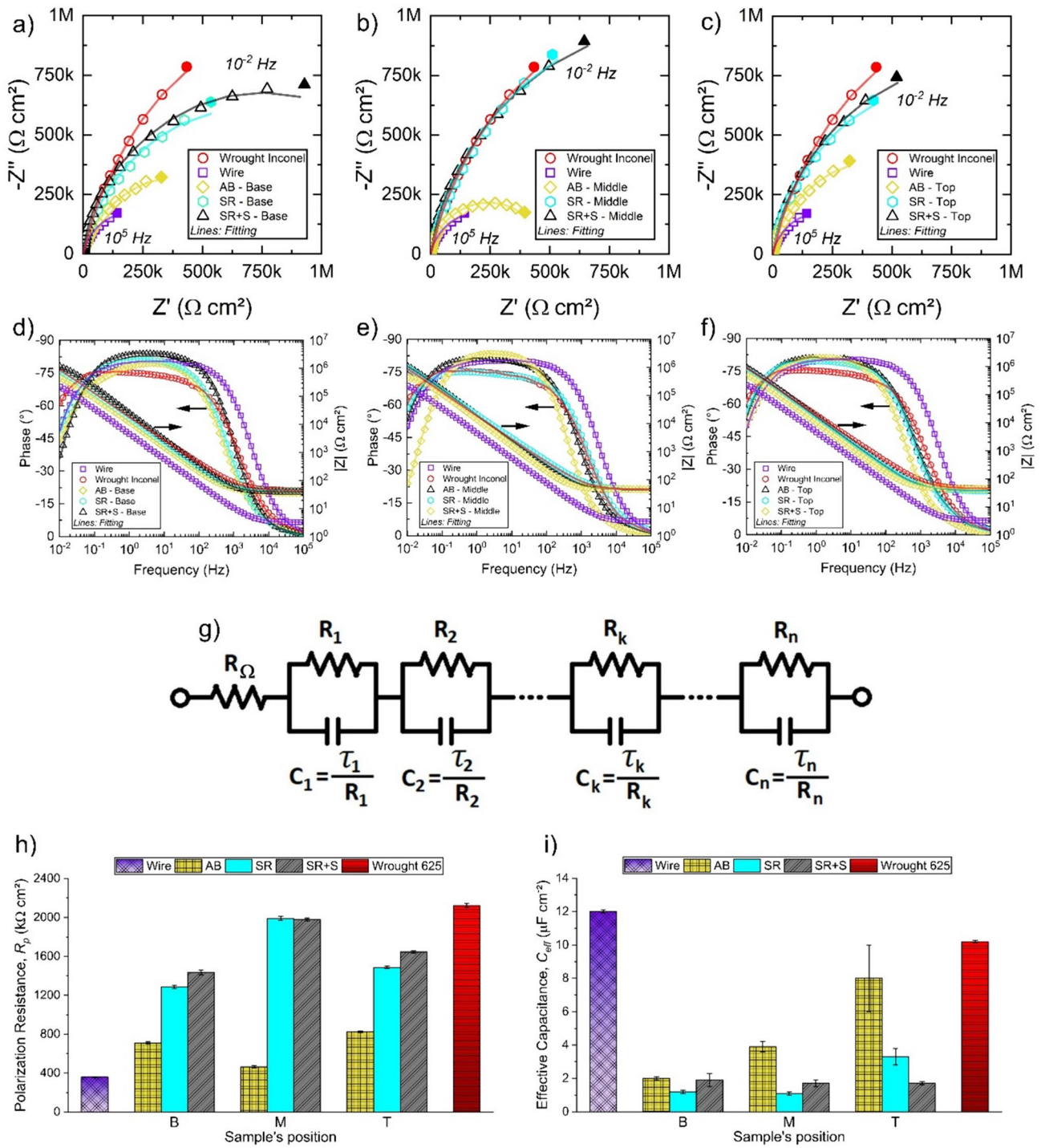


Fig. 11 Nyquist plots from **a** base, **b** middle, and **c** top regions of samples at AB, SR, and SR+S conditions. Bode phase ($^\circ$) and $|Z|$ ($\Omega \text{ cm}^2$) plots from **d** base, **e** middle, and **f** top regions of samples at AB, SR, and SR+S conditions. Experimental impedance data indicated as the symbol and the fitting as solid lines from the

Measurement Model regression approach using **g** a series of Voigt elements (a resistance in parallel to a capacitor). **h** Polarization resistance, R_p , and **i** effective capacitance, C_{eff} , from the Measurement Model Approach to interpreting the experimental EIS data

anodic polarization exceeding the transpassive potential, the surface of the samples was covered by oxide scales enriched in corrosion-resistant elements, as shown in Fig. 12b, and

reduced and small pits underneath the oxides, Fig. 12. The oxide layer formed on the surface after polarization was discontinuous, exposing the base metal, whose composition

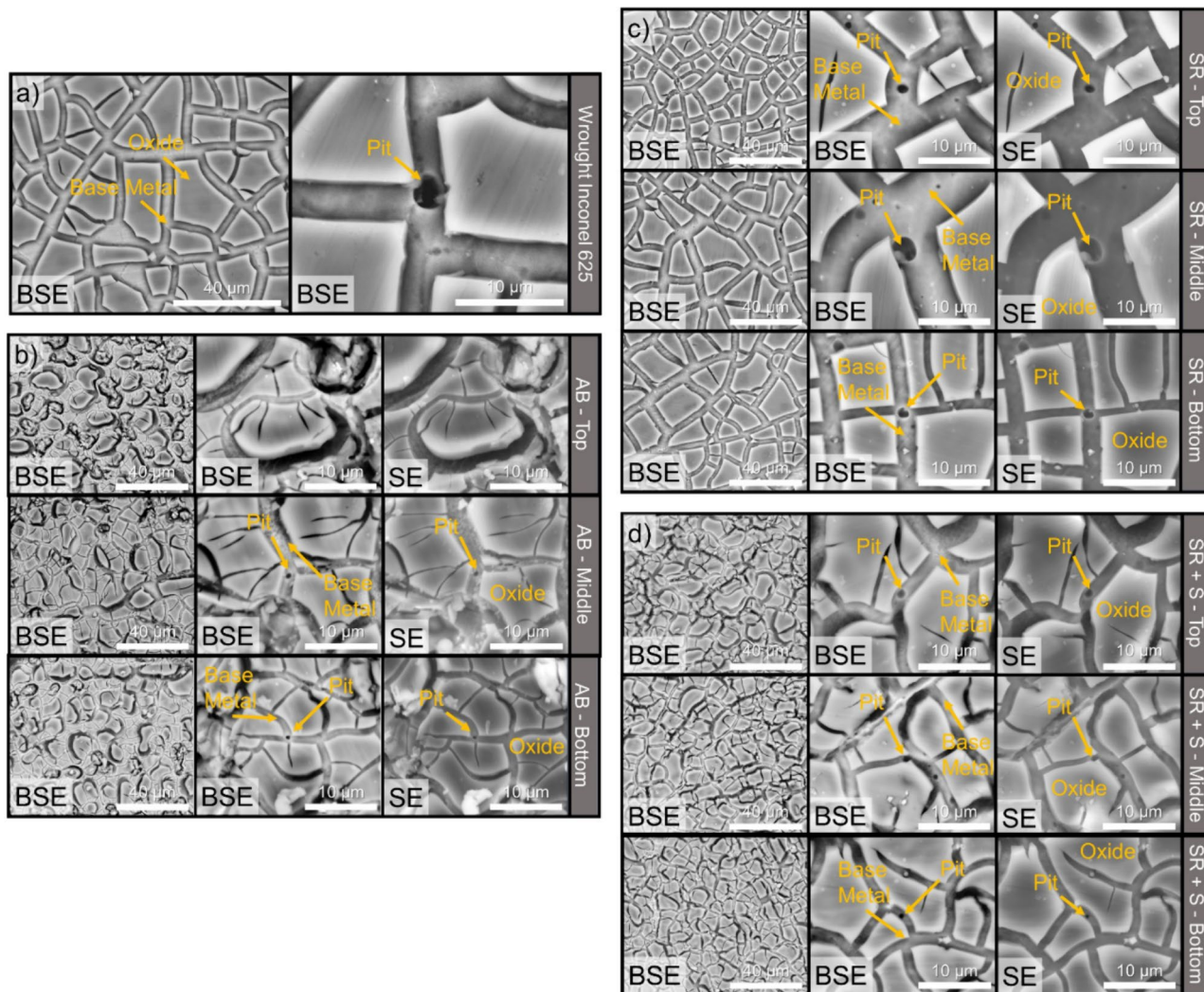


Fig. 12 Surfaces of **a** Wrought IN625 and DED-WA-processed IN625 at **b** AB, **c** SR, and **d** SR+S region following anodic polarization in substitutive seawater in different regions: Top, Middle, and

Bottom. BSE and SE represent backscattered and secondary electron micrographs from SEM analyses

was similar regardless of the sample condition, Fig. 13. The post-polarization surface of the wrought 625 alloy, Fig. 12a, was identical to the alloys at different conditions: AB, Fig. 12b, SR, Fig. 12b, and SR+S, Fig. 12c.

Table 5 and Fig. 14 show the results of the ASTM G48-11 (2020) for a sample immersed 72 h at 50 °C. This standard refers to the pitting and crevice corrosion resistance of stainless steels and related alloys using ferric chloride solubilization. In the present study, some pits were found in the AB condition in the middle position (Fig. 14), while the SR+S condition did not present pitting and SR pitting in all the positions. These results mean that the AB condition can develop pits depending on the thermal history. Applying only the SR treatment is not recommended because it reduces the material’s corrosion resistance and should be

complemented using a solubilization treatment. Therefore, toughness and corrosion resistance can be improved.

4 Discussion

Figure 15 summarizes our study’s ultimate tensile strength (UTS) and elongation at fracture (ELF) and other studies for comparison. In the present study, although the results of hardness and tensile tests presented a dispersion, there is not a significant variation between the three assessed regions: bottom, middle, and top. Nonetheless, some conditions of the horizontal tensile samples in the bottom depicted slightly higher UTS values than the middle and top. Some authors mention that boundary strengthening

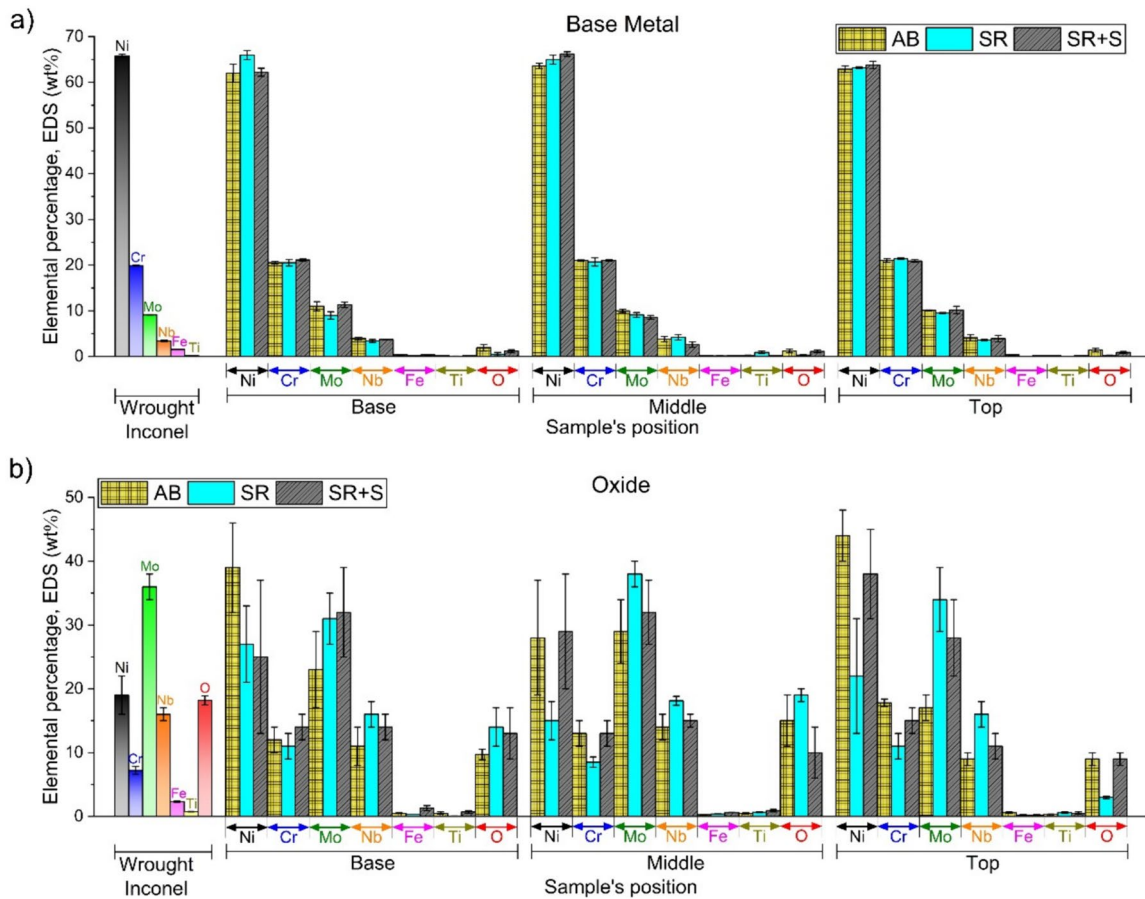


Fig. 13 EDS analyses presented as mean values and their deviations from 03 different oxide and base metal regions indicated in Fig. 12

Table 5 Corrosion results according to the ASTM G48-11 (2020) for sample immersed 72 h at 50 °C

Sample	Position	Area (m ²)	Weight (g)		Weight loss (g/m ²)	Pitting corrosion
			Initial	Final		
AB	Top	0.00202	41.31200	41.31200	0.00000	Free
	Middle	0.00186	38.38500	38.36780	9.23234	Found
	Bottom	0.00177	31.49470	31.49440	0.16965	Free
SR	Top	0.00106	29.01600	29.01300	2.82540	Found
	Middle	0.00181	36.58040	36.57990	0.27657	Found
	Bottom	0.00154	28.97300	28.96200	7.13597	Found
SR+S	Top	0.00205	43.94100	43.94100	0.00000	Free
	Middle	0.00178	37.18540	37.18540	0.00000	Free
	Bottom	0.00236	50.35510	50.35510	0.00000	Free

and Laves phase close to the bottom might cause variation [38].

The as-built conditions presented the lowest ultimate tensile strength (UTS), with values around 716 MPa and elongations at fracture of approximately 40% in the vertical and horizontal directions. Other authors, using DED-WA with CMT equipment and changing the building parameters, have reported values around 648–687 MPa

and elongation of 46–43% [24], and in another study, UTS from 693 to 751 MPa and maximum elongations at fracture of 60% [38], UTS below 750 MPa and ELF higher than 40% [7]. Bon et al. [14], using a similar alloy processed by DED-LB and similar heat treatments to assess the horizontal and vertical orientations, show UTS values between 850 and 1025 MPa and elongation to fracture between 15 and 38%. Jiang et al. [38] show

Fig. 14 Corrosion results according to the ASTM G48-11 (2020) for samples immersed 72 h at 50 °C

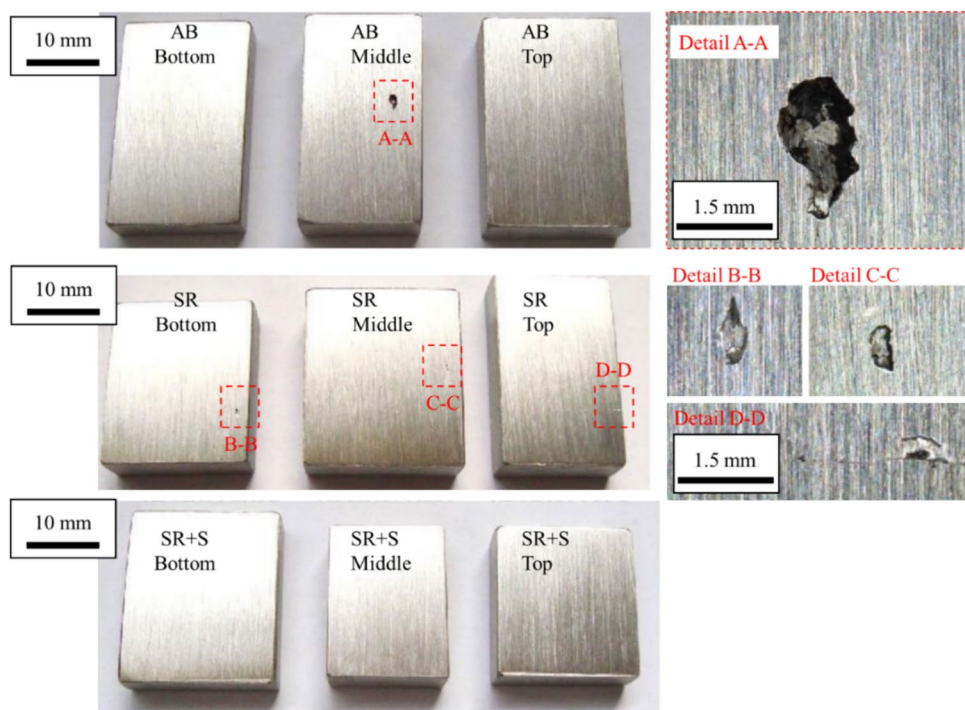
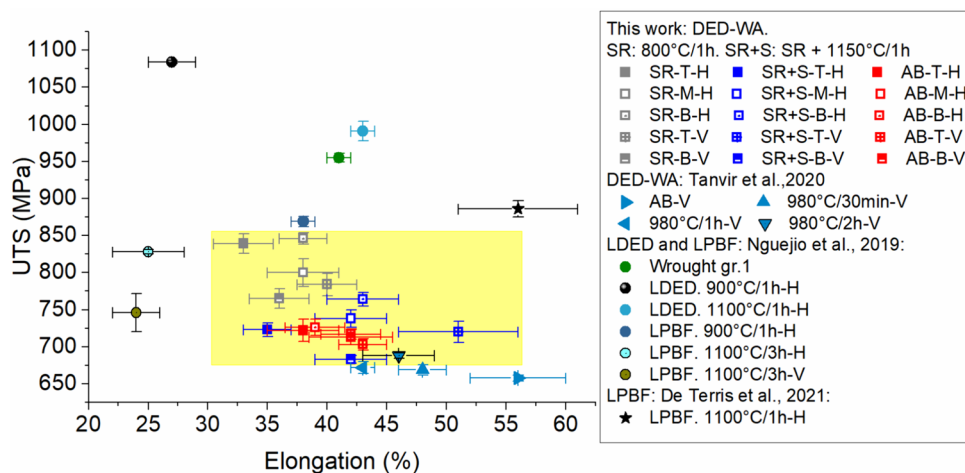


Fig. 15 Summary of tensile results of the present work and some other references (Tanvir et al. [7], Nguejio et al. [39] and De Terris et al. [40]). Some tests were conducted in the horizontal (H) and vertical (V) directions in the as-build (AB) and heat-treated samples



an interesting comparison between different additive manufacturing processes, highlighting the differences in mechanical properties. Therefore, the mechanical response of the as-build condition depends on the fabrication parameters since the thermal cycle in each layer depends on the amount of heat added to the component, the substrate, the layer height, the height from the substrate to the working layer, and the cooling configuration during the manufacturing.

After the heat treatments, no evidence of changes in the microstructure was found after the stress relief (SR). However, we saw improvement in mechanical properties

and a reduction of the ELF compared to the AB condition. The ELF was observed between 30 and 45%, and the fracture toughness was reduced by approximately half of that from the AB condition. Nevertheless, precipitation was observed due to changes in the lattice parameter and increased hardness. However, this precipitation of the δ -phase should have been low since we could not see evidence of this formation on the X-ray diffraction (XRD). Lass et al. [19], using neutron diffraction, show that stress relief treatments at 800 °C for 1 h are ideal for PBF-LB in the IN625; however, after 4 h, there was evidence of δ -phase precipitation observed by XRD, which can be deleterious

to ductility and corrosion of welded joints [17] and clad materials [18]. An interesting evolution of the δ -phase and the reduction of the lattice parameters of the γ -phase in the IN625 processed by DED-AW, using synchrotron radiation, is shown by Rodrigues et al. [5].

After the solution treatment, the microstructure suffered changes, the mechanical strength decreased, and the capacity to absorb plastic deformation increased, evidenced by the increment of ELF and fracture toughness. Once again, as observed in Fig. 15, solution treatments at 900 °C for 1 h favored the formation of the δ -phase and increased the UTS, while solution treatments at 1100 °C for 1 h reduced the UTS and increased the ELF. Fullen et al. [20] It was also found that SR was the hardest condition, while the solubilization softened the matrix. However, the thermal history of the component could change the phases' kinetics, for example, De Terris et al. [40], with a solubilized condition with larger UTS and ELF than the described conditions. Although a solution treatment at 1150 °C for 1 h can solubilize all the phases, MC-type carbides can form during cooling [5].

The CTOD values in our study were, on average, 1.5 mm for the AB, 0.7 mm for the SR, and 1.8 mm for the SR + S conditions where except by the SR, toughness results are superior to the wrought IN625, around 0.75 – 0.93 mm [41]. No published studies have dealt with this material processed by additive manufacturing to compare with fracture toughness; however, Puppala et al. [42] used rapid laser manufacturing with laser and powder feedstock to deposit V-grooved like-welds. They found CTOD values between 0.28 – 0.4 mm for the as-built condition and 0.34–0.54 mm for the heat-treated condition (950 °C for 1 h), while Yeni et al. [41] reported CTOD values between 0.53 and 0.88 mm for the fusion zone and 0.71–0.83 mm for the heat-affected zone in welded joints; in any case, values below the results reported for the base metal 0.75–0.93 mm [41].

Although a solid solution strengthens alloys, IN625 usually requires post-treatment in the as-built condition to achieve an optimum basket of properties [43]. Some studies have shown that the corrosion properties are sensitive to heat treatment [10] and the complex precipitation behavior is highly related to temperature and time [44]. The repeated heating cycles of additive manufacturing processes may induce precipitates within the microstructure of IN625, such as the Laves phase, δ -phase, γ' -phase, TiN, and carbides [45, 46].

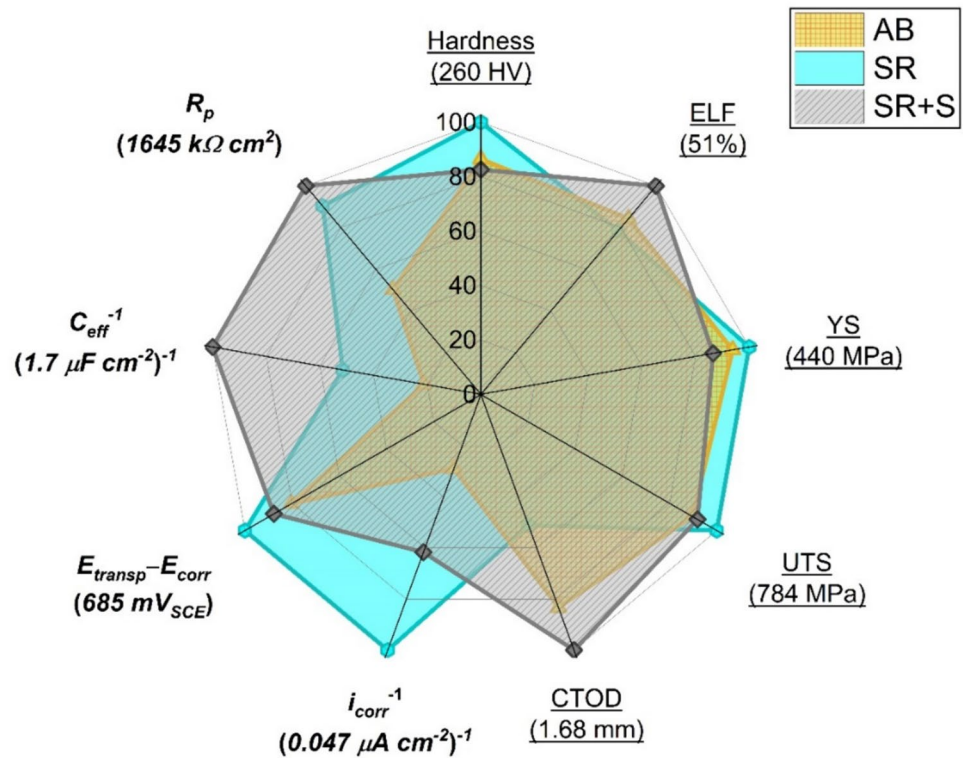
Our study demonstrated that, even in the as-built conditions, the corrosion resistance of the DED-WA-produced samples was superior to that of the wire consumable alloy, and at the SR and SR + S conditions displayed similar corrosion resistance to the commercial wrought IN625 included as comparison, Figs. 10 and 11. Heat treatments at 800 °C and 1100 °C for 1 h impacted the corrosion resistance of the alloys. Despite all alloys being

corrosion resistant, the AB alloy displayed lower corrosion resistance than the SR and SR + S alloys when tested in synthetic seawater. However, when tested in ferritic chloride solution for 72 h at 50 °C, the SR + S alloys performed better among the tested DED-WA-produced alloys, with negligible weight loss and free of visual localized corrosion, such as pitting formation.

Zhao et al. have shown heat treatment's effect on IN625 samples fabricated by WAAM [47] by potentiodynamic polarization. A balance of a decrease in dislocation density (stress relief) and dissolution of deleterious phases (solubilization), without precipitating other harmful phases, is desired to improve corrosion resistance. However, finding the narrow-optimized heat treatment conditions is challenging, with the superposition of the phenomena mentioned before resulting in a lack of consensus or inconsistency of results between different studies. Additive manufactured IN625 has often been characterized for its heterogeneous thermal characteristics, inducing spatial heterogeneity within the microstructure and properties. This aspect brings difficulties to ensuring a post-heating treatment that avoids complex precipitation fields of deleterious phases and enables tailored and homogeneous microstructures. As far as the corrosion resistance is concerned, SR + S alloys are recommended since they present high resistance in seawater: low i_{corr} ($< 0.1 \mu\text{A cm}^{-2}$), high $E_{transp} - E_{corr}$ ($> 600 \text{ mV}$), high R_p ($> 10^6 \Omega \text{ cm}^2$), low C_{eff} ($< 2 \mu\text{F cm}^{-2}$), and resistance in aggressive ferritic chloride solution for 72 h at 50 °C, with negligible weight loss and no sign of pitting corrosion. AB and SR alloys also retained appreciable corrosion resistance in synthetic seawater but failed to completely suppress the localized corrosion in aggressive ferritic chloride solution. After polarization in seawater, the SR + S alloy, like the AB and SR ones, displayed a compact but discontinuous corrosion product layer with small pits underneath, i.e., with low associated damage along anodic polarization. However, pit formation was found at AB and SR state after exposure to ferritic chloride solution for 72 h at 50 °C.

The radar chart depicted in Fig. 16 is convenient for summarizing and comparing multiple mechanical and electrochemical properties of the DED-WA-processed alloys in the top region at different conditions: AB, SR, SR + S. Selected mechanical and electrochemical parameters were evaluated in concert to discuss which alloy condition presents the most favorable combination of properties. The best properties are located at the vertex of the plot, where the hypothetical material would be the hardest, strongest, toughest, and most corrosion resistant. Among the conditions, the AB alloy is the least favorable since this condition does not ensure any optimized mechanical or electrochemical properties. SR alloy displayed reasonable electrochemical properties ($i_{corr} \sim 0.047 \mu\text{A cm}^{-2}$ and $E_{transp} - E_{corr} \sim 685 \text{ mV}_{SCE}$). It was the strongest

Fig. 16 Radar plot combining the experimentally determined mechanical and electrochemical attributes of the top region of the DED-WA-produced alloys at AB, SR, and SR + S conditions. Boundary values in parentheses () are assumed to be 100% and are taken as the mean values from Figs. 4, 7, 8, 10 and 11. Reciprocal i_{corr} and C_{eff} allow a straightforward interpretation of the best properties in the plot's corners. Electrochemical parameters are highlighted in italics, and mechanical properties are underlined



(YS ~ 440 MPa and UTS ~ 784 MPa) but at the expense of the elongation (EL ~ 40%) and fracture toughness (CTOD ~ 0.86 mm). Relying on a single property or characteristic does not meet the strict requirements expected for components produced with Ni-based superalloys. Despite the mechanical and corrosion resistance attributes, damage tolerance is a crucial parameter to be considered. Among the alloys' conditions, the SR + S exhibits the best portfolio of properties, as appraised in the expanded chart, indicating an alloy still strong and corrosion resistant with the benefit of being tolerant to damage (the highest EL and CTOD attributes).

5 Conclusion

- Thin-walled components 210 × 100 × 60 mm and 10 mm were successfully fabricated by wire arc additive manufacturing through the direct energy deposition (DED-WA) technique, specifically using gas metal arc welding with regulated metal deposition (GMAW—RMD™) of IN625. After a parameter's development, a condition offering non-macroscopic defects was chosen.
- The as-build conditions presented ultimate tensile strength (716 MPa), large elongations at fracture (≥ 35%), and intermediate fracture toughness (> 1.25 mm). Anisotropy is also observed between the vertical and horizontal direction, even in the heat treatment.

- The stress relief (SR) heat treatment improved mechanical properties (YS of ~ 450 MPa and UTS of ~ 750 MPa). However, the lowest elongation at fracture and fracture toughness (≥ 30% and > 0.5 mm) were presented. On the other hand, the additional solution treatment (SR + S) improved the elongation at fracture and fracture toughness (≥ 30% and > 1.5 mm) regarding the AB and SR conditions. Yet, the mechanical strength was similar to the AB condition.
- The corrosion resistance of all the conditions was higher than that shown by the wire and comparable to that of the wrought IN625 alloy at the SR and SR + S conditions. The immersion corrosion test showed that the SR + S condition did not present weight loss or pitting after 72 h of the test.
- When assessed in concert, the mechanical *versus* electrochemical parameters highlight the favorable strength, toughness, and corrosion resistance of the DED-WA IN625 alloy after SR + S.

Acknowledgements The support of the Center for Research and Innovation in Materials and Structures (CEPIMATE) is deeply appreciated. This research used facilities of the Brazilian Nanotechnology National Laboratory (LNNano), part of the Brazilian Centre for Research in Energy and Materials (CNPEM), a private non-profit organization under the supervision of the Brazilian Ministry for Science, Technology, and Innovations (MCTI). The Electron Microscopy Laboratory staff are acknowledged for their assistance during the experiments (proposal SEM-FIB-C1-20233619).

Funding Funded by Fundação de Amparo à Pesquisa do Estado de São Paulo (Grant No. 20/09079-2), Thiago Roberto Felisardo Cavalcante recognizes the financial support through the Ph.D. scholarship from the Coordenação de Aperfeiçoamento de Pessoal de Nível Superior – Brasil (CAPES) – Finance Code 001. J.P. Oliveira acknowledges the funding by national funds from FCT - Fundação para a Ciência e a Tecnologia, I.P., in the scope of the projects LA/P/0037/2020, UIDP/50025/2020 and UIDB/50025/2020 of the Associate Laboratory Institute of Nanostructures, Nanomodelling and Nanofabrication – i3N. E.S.N. Lopes acknowledges the funding by University of Campinas, Dean of Research, PIND – Programa de Incentivo a Novos Docentes da Unicamp (Grant #2580/23). J.A. Avila is a CNPq fellow (Conselho Nacional de Desenvolvimento Científico e Tecnológico) under grant #306960/2021-4.

Data availability The data supporting this study's findings are available from the corresponding author, J. A. Avila, upon reasonable request.

Declarations

Conflict of interest statement The authors declare that they have no known competing financial interests or personal relationships that could have appeared to influence the work reported in this paper.

References

- Rodrigues TA, Duarte V, Miranda RM, Santos TG, Oliveira JP (2019) Current status and perspectives on wire and arc additive manufacturing (WAAM). *Materials* 12:1121. <https://doi.org/10.3390/ma12071121>
- Dutta B, Babu S, Jared B (2019) Science, technology and applications of metals in additive manufacturing. Elsevier. <https://doi.org/10.1016/C2017-0-04707-9>
- Shankar V, Bhanu Sankara Rao K, Mannan SL (2001) Microstructure and mechanical properties of Inconel 625 superalloy. *J Nucl Mater* 288: 222–232. [https://doi.org/10.1016/S0022-3115\(00\)00723-6](https://doi.org/10.1016/S0022-3115(00)00723-6)
- Shoemaker LE (2005) Alloys 625 and 725: Trends in Properties and Applications, in: *Superalloys 718, 625, 706 and Various Derivatives* (2005), TMS, pp. 409–418. https://doi.org/10.7449/2005/Superalloys_2005_409_418
- Rodrigues TA, Cipriano Farias FW, Avila JA, Maawad E, Schell N, Santos TG, Oliveira JP (2023) Effect of heat treatments on Inconel 625 fabricated by wire and arc additive manufacturing: an in situ synchrotron X-ray diffraction analysis. *Sci Technol Welding Joining* 1–6. <https://doi.org/10.1080/13621718.2023.2187927>
- Farias FWC, Duarte VR, Felice IO, da Filho JCP, Schell N, Maawad E, Avila JA, Li JY, Zhang Y, Santos TG, Oliveira JP (2023) In situ interlayer hot forging arc-based directed energy deposition of Inconel® 625: process development and microstructure effects. *Addit Manuf* 66: 103476. <https://doi.org/10.1016/j.addma.2023.103476>
- Tanvir ANM, Ahsan MRU, Seo G, Kim J, Ji C, Bates B, Lee Y, Kim DB (2020) Heat treatment effects on Inconel 625 components fabricated by wire + arc additively manufacturing (WAAM)—part 2: mechanical properties. *Int J Adv Manuf Technol* 110:1709–1721. <https://doi.org/10.1007/s00170-020-05980-w>
- Tanvir ANM, Ahsan MdRU, Ji C, Hawkins W, Bates B, Kim DB (2019) Heat treatment effects on Inconel 625 components fabricated by wire + arc additive manufacturing (WAAM)—part 1: microstructural characterization. *Int J Adv Manuf Technol* 103:3785–3798. <https://doi.org/10.1007/s00170-019-03828-6>
- S. Dongari, M.J. Davidson, Multi response optimization of Inconel 625 wire arc deposition for development of additive manufactured components using Grey relational analysis (GRA), *Metallurgical Mater Eng* 27 (2021) 177–192. <https://doi.org/10.30544/586>
- Sharma H, Singla J, Singh V, Singh J, Kumar H, Bansal A, Singla AK, Goyal DK, Gupta MK (2023) Influence of post heat treatment on metallurgical, mechanical, and corrosion analysis of wire arc additive manufactured inconel 625. *J Market Res* 27:5910–5923. <https://doi.org/10.1016/j.jmrt.2023.11.074>
- Prajapati V, Dinbandhu JJ, Vora S, Das K (2020) Abhishek, study of parametric influence and welding performance optimization during regulated metal deposition (RMD™) using grey integrated with fuzzy taguchi approach. *J Manuf Process* 54:286–300. <https://doi.org/10.1016/j.jmapro.2020.03.017>
- Gradl PR, Protz C, Wammen T Additive manufacturing development and hot-fire testing directed energy deposition inconel 625 and JBK-75 alloys, 55th AIAA/SAE/ASSEE joint propulsion conference 2019 (2019) 1–20.
- ASM International, *Heat Treater's Guide: Practices and Procedures for Nonferrous Alloys*, ASM International (1996) 657.
- Bon D, Cavalcante T, Thiesen A, Santos H, Gutjahr J, Cintho O, Coelho R, de Oliveira MF, Ribamar GG, Avila JA (2024) Effect of stress relief and solubilization heat treatments on laser additive manufactured Inconel 625: microstructure and properties. *Int J Adv Manuf Technol*. <https://doi.org/10.1007/s00170-024-12967-4>
- Stoudt MR, Lass EA, Ng DS, Williams ME, Zhang F, Campbell CE, Lindwall G, Levine LE (2018) The influence of annealing temperature and time on the formation of δ -phase in additively-manufactured inconel 625. *Metall Mater Trans A* 49:3028–3037. <https://doi.org/10.1007/s11661-018-4643-y>
- Liu X, Fan J, Zhang P, Cao K, Wang Z, Chen F, Liu D, Tang B, Kou H, Li J (2023) Influence of heat treatment on Inconel 625 superalloy sheet: carbides, γ' , δ phase precipitation and tensile deformation behavior. *J Alloys Compd* 930:167522. <https://doi.org/10.1016/j.jallcom.2022.167522>
- Cortial F, Corrieu JM, Vernot-Loier C (1995) Influence of heat treatments on microstructure, mechanical properties, and corrosion resistance of weld alloy 625. *Metall Mater Trans A* 26:1273–1286. <https://doi.org/10.1007/BF02670621>
- Guo L, Xiao F, Wang F, Wei W, He Y, Luo F (2020) Influence of heat treatments on microstructure, mechanical properties and corrosion resistance of Inconel 625 overlay clad using PTIG. *Mater Res Express* 7:096517. <https://doi.org/10.1088/2053-1591/abb858>
- Lass EA, Stoudt MR, Williams ME, Katz MB, Levine LE, Phan TQ, Gnaeupel-Herold TH, Ng DS (2017) Formation of the Ni3Nb δ -phase in stress-relieved inconel 625 produced via laser powder-bed fusion additive manufacturing. *Metall Mater Trans A* 48:5547–5558. <https://doi.org/10.1007/s11661-017-4304-6>
- Fullen MD, Schneider JA (2019) Effects of varying heat treatments on the microstructure and mechanical properties of blown powder inconel 625. *Jom* 71:1127–1133. <https://doi.org/10.1007/s11837-019-03339-5>
- ASTM, Standard Specification for Nickel-Chromium-Molybdenum-Niobium Alloy, Nickel-Chromium-Molybdenum-Silicon Alloy, and Nickel-Chromium-Molybdenum-Tungsten Alloy Rod and Bar, B446-23, 2023. <https://doi.org/10.1520/B0446-23>
- ASTM, Standard Specification for Additive Manufacturing Nickel Alloy (UNS N06625) with Powder Bed Fusion, F3056-14 (Reapproved 2021), 2021. <https://doi.org/10.1520/F3056-14R21>
- Raja M, Tiwari Y, Mukherjee M, Maji B, Chatterjee A (2022) Effect of bidirectional and switchback deposition strategies on microstructure and mechanical properties of wire arc additive

- manufactured Inconel 625. *Int J Adv Manuf Technol* 119:4845–4861. <https://doi.org/10.1007/s00170-022-08687-2>
24. Yangfan W, Xizhang C, Chuanchu S (2019) Microstructure and mechanical properties of Inconel 625 fabricated by wire-arc additive manufacturing. *Surf Coat Technol* 374:116–123. <https://doi.org/10.1016/j.surfcoat.2019.05.079>
 25. Dubiel B, Sieniawski J (2019) Precipitates in additively manufactured inconel 625 superalloy. *Materials* 12:1–11. <https://doi.org/10.3390/ma12071144>
 26. Wang Y, Chen X (2019) Investigation on the microstructure and corrosion properties of Inconel 625 alloy fabricated by wire arc additive manufacturing. *Mater Res Express* 6:106568. <https://doi.org/10.1088/2053-1591/ab39f6>
 27. Xing X, Di X, Wang B (2014) The effect of post-weld heat treatment temperature on the microstructure of Inconel 625 deposited metal. *J Alloys Compd* 593:110–116. <https://doi.org/10.1016/J.JALLCOM.2013.12.224>
 28. Drouin D, Couture AR, Joly D, Tastet X, Aimez V, Gauvin R (2007) CASINO V2.42—A fast and easy-to-use modeling tool for scanning electron microscopy and microanalysis users, scanning 29: 92–101. <https://doi.org/10.1002/sca.20000>
 29. Watson W, Orazem ME (2020) EIS: Measurement Model Program, Can Be Found under Ecsarxiv.Org/Kze9x.
 30. Liao H, Watson W, Dizon A, Tribollet B, Vivier V, Orazem ME (2020) Physical properties obtained from measurement model analysis of impedance measurements. *Electrochim Acta*. <https://doi.org/10.1016/j.electacta.2020.136747>
 31. Barroux A, Delgado J, Orazem ME, Tribollet B, Laffont L, Blanc C (2021) Electrochemical impedance spectroscopy study of the passive film for laser-beam-melted 17–4PH stainless steel. *Corros Sci* 191. <https://doi.org/10.1016/j.corsci.2021.109750>
 32. Antonsson T, Fredriksson H, The Effect of Cooling Rate on the Solidification of INCONEL 718, n.d.
 33. Diepold B, Vorlaufer N, Neumeier S, Gartner T, Göken M (2020) Optimization of the heat treatment of additively manufactured Ni-base superalloy IN718. *Int J Miner Metall Mater* 27:640–648. <https://doi.org/10.1007/s12613-020-1991-6>
 34. Petrzak P, Kowalski K, Blicharski M (2016) Analysis of phase transformations in inconel 625 alloy during annealing. *Acta Phys Pol A* 130: 1041–1044. <https://doi.org/10.12693/APhysPolA.130.1041>
 35. Karmuhilan M, Somasundaram K (2023) Microstructural features and corrosion behavior of Inconel 625 components fabricated using Wire and Arc Additively Manufacturing (WAAM). *Weld Int* 37:617–625. <https://doi.org/10.1080/09507116.2023.2269087>
 36. Engelhardt GR, Case RP, Macdonald DD (2016) Electrochemical impedance spectroscopy optimization on passive metals. *J Electrochem Soc* 163:C470–C476. <https://doi.org/10.1149/2.0811608jes>
 37. Benoit M, Bataillon C, Gwinner B, Miserque F, Orazem ME, Sánchez-Sánchez CM, Tribollet B, Vivier V (2016) Comparison of different methods for measuring the passive film thickness on metals. *Electrochim Acta* 201:340–347. <https://doi.org/10.1016/j.electacta.2015.12.173>
 38. Jiang Q, Zhang P, Yu Z, Shi H, Li S, Wu D, Yan H, Ye X, Chen J (2021) Microstructure and mechanical properties of thick-walled inconel 625 alloy manufactured by wire arc additive manufacture with different torch paths. *Adv Eng Mater* 23. <https://doi.org/10.1002/adem.202000728>
 39. Nguejio J, Szmytka F, Hallais S, Tanguy A, Nardone S, Godino Martinez M (2019) Comparison of microstructure features and mechanical properties for additive manufactured and wrought nickel alloys 625. *Materials Science and Engineering: A* 764: 138214. <https://doi.org/10.1016/J.MSEA.2019.138214>
 40. De Terris T, Castelnau O, Hadjem-Hamouche Z, Haddadi H, Michel V, Peyre P (2021) Analysis of as-built microstructures and recrystallization phenomena on inconel 625 alloy obtained via laser powder bed fusion (L-PBF). *Metals (Basel)* 11:619. <https://doi.org/10.3390/met11040619>
 41. Yeni C, Koçak M (2006) Fracture toughness analysis of laser-beam-welded superalloys Inconel 718 and 625. *Fatigue Fract Eng Mater Struct* 29:546–557. <https://doi.org/10.1111/j.1460-2695.2006.01025.x>
 42. Puppala G, Moitra A, Sathyanarayanan S, Kaul R, Sasikala G, Prasad RC, Kukreja LM (2014) Evaluation of fracture toughness and impact toughness of laser rapid manufactured Inconel-625 structures and their co-relation. *Mater Des* 59:509–515. <https://doi.org/10.1016/j.matdes.2014.03.013>
 43. Kong Y, Huang H (2022) Effect of intrinsic heat treatment on microstructure and hardness of additively manufactured Inconel 625 alloy by directed energy deposition. *Mater Des* 224:111279. <https://doi.org/10.1016/j.matdes.2022.111279>
 44. Marchese G, Lorusso M, Parizia S, Bassini E, Lee J-W, Calignano F, Manfredi D, Terner M, Hong H-U, Ugues D, Lombardi M, Biamino S (2018) Influence of heat treatments on microstructure evolution and mechanical properties of Inconel 625 processed by laser powder bed fusion. *Mater Sci Eng, A* 729:64–75. <https://doi.org/10.1016/j.msea.2018.05.044>
 45. Silva CC, De Miranda HC, Motta MF, Farias JP, Afonso CRM, Ramirez AJ (2013) New insight on the solidification path of an alloy 625 weld overlay. *J Market Res* 2:228–237. <https://doi.org/10.1016/j.jmrt.2013.02.008>
 46. Zhang W, Xu Y, Shi Y, Su G, Gu Y, Volodymyr K (2022) Intergranular corrosion characteristics of high-efficiency wire laser additive manufactured Inconel 625 alloys. *Corros Sci* 205. <https://doi.org/10.1016/j.corsci.2022.110422>
 47. Zhao X, Di X, Zhang X, Li C (2021) Improvement in corrosion resistance of wire arc additive manufactured Inconel 625 alloy through heat treatment. *Mater Res Express* 8. <https://doi.org/10.1088/2053-1591/ac0b0b>

Publisher's Note Springer Nature remains neutral with regard to jurisdictional claims in published maps and institutional affiliations.

Springer Nature or its licensor (e.g. a society or other partner) holds exclusive rights to this article under a publishing agreement with the author(s) or other rightsholder(s); author self-archiving of the accepted manuscript version of this article is solely governed by the terms of such publishing agreement and applicable law.